



## Research paper

# Distinct types of C-H-O-N atmospheres and surface pressures depending on melt redox state and outgassing efficiency

Caroline Brachmann <sup>a,b</sup> ,\* Lena Noack <sup>b</sup> , Philipp Alexander Baumeister <sup>b</sup> , Frank Sohl <sup>a</sup> 

<sup>a</sup> Institute of Planetary Research, German Aerospace Center (DLR), Rutherfordstr. 2, Berlin, 12489, Germany

<sup>b</sup> Institute of Geological Sciences, Freie Universität Berlin, Malteserstr. 74 - 100, Berlin, 12249, Germany

## ARTICLE INFO

## Keywords:

Planetary atmospheres  
Atmospheric composition  
Volcanism

## ABSTRACT

After the magma ocean state, secondary atmospheres build up via early volcanic degassing of planetary interiors. The terrestrial planets Venus, Earth, and Mars are believed to have originated from similar source material but reveal distinct present-day atmospheric compositions, pressures, and temperatures. To investigate how such diverse atmospheres emerge, we have built a three-step model coupling mantle and atmospheric composition. The model incorporates mantle melting, melt ascent, and volcanic degassing. Additionally, it includes atmospheric equilibrium chemistry, taking into account processes such as water condensation and hydrogen escape. Key parameters such as mantle oxygen fugacity, melt production rates, surface temperature, and volatile abundance in the mantle, were varied to understand their impact on atmospheric composition and pressure. For reduced mantles with redox states below IW +1, atmospheric pressures remain strongly limited to a maximum of 2 bar due to the outgassing of predominantly light species that are prone to atmospheric escape or condensation. Above IW +1, atmospheric pressure can reach several tens of bars depending on the outgassing efficiency. For high-pressure atmospheres, CO<sub>2</sub> is the main atmospheric species observed in our models. For oxidized low-pressure atmospheres, depending on temperature, atmospheres can be either water-rich or also CO<sub>2</sub>-dominated. For reducing atmospheres, nitrogen species tend to dominate the atmospheres, with NH<sub>3</sub> for colder atmospheres and N<sub>2</sub> for warmer atmospheres. CH<sub>4</sub> becomes dominant only in a narrow parameter space at redox states around IW +0.5 to IW +2 and is favored by lower atmospheric temperatures.

## 1. Introduction

The planets and moons in the solar system exhibit a wide range of atmospheric compositions and surface conditions (summarized in Table 1), prompting questions about whether these variations arose from different initial conditions or if they may represent different evolutionary pathways. Some authors argue that the formation of terrestrial planets resulted from gravitational scattering, with materials originating across the entire spectrum of terrestrial planet orbits, thereby suggesting similar initial inventories for Venus, Earth, and Mars (Walsh and Morbidelli, 2011; O'Brien et al., 2014). However, others propose that their positions in the accretion disc had a great impact on their bulk composition, with water-bearing minerals potentially not condensing in high-temperature regions within 1 AU, i.e., potentially leading to Venus being depleted of water (Albarède, 2009).

Calcium-aluminium-rich inclusions (CAIs) in some of the most primitive meteorites suggest the incorporation of a substantial amount of interstellar water during the initial stages of protosolar cloud evolution,

implying the early formation of planetary reservoirs enriched in volatile elements (Aléon et al., 2022). Consequently, materials in the early Solar System containing volatiles would have contributed to the building blocks of the rocky planets, such as pebbles (e.g., Morbidelli et al., 2012; Raymond, 2021; Johansen et al., 2021), and/or planetesimals (Chambers and Wetherill, 1998; Burkhardt et al., 2021).

Some authors propose that Earth's water and volatiles could have been delivered by volatile-rich carbonaceous chondrites, initially formed beyond Jupiter's orbit but displaced inward in the course of planetary growth and migration (Kleine et al., 2020). Marty (2012) suggests that isotope signatures of terrestrial H, N, Ne, and Ar result from mixing between two endmembers of solar and chondritic compositions.

The latter case with volatiles arriving lately, after or during the disc's dispersal is broadly accepted for the origin of volatiles in the inner Solar System (Morbidelli et al., 2000; Raymond et al., 2004; O'Brien et al., 2006; Raymond et al., 2009; Walsh et al., 2011; Raymond and Izidoro, 2017; Ronco and de Elía, 2018), which may also play a role

\* Corresponding author at: Institute of Planetary Research, German Aerospace Center (DLR), Rutherfordstr. 2, Berlin, 12489, Germany.

E-mail addresses: [caroline.brachmann@dlr.de](mailto:caroline.brachmann@dlr.de) (C. Brachmann), [lena.noack@fu-berlin.de](mailto:lena.noack@fu-berlin.de) (L. Noack), [philipp.baumeister@fu-berlin.de](mailto:philipp.baumeister@fu-berlin.de) (P.A. Baumeister), [frank.sohl@fu-berlin.de](mailto:frank.sohl@fu-berlin.de) (F. Sohl).

<https://doi.org/10.1016/j.icarus.2024.116450>

Received 15 July 2024; Received in revised form 15 December 2024; Accepted 18 December 2024

Available online 3 January 2025

0019-1035/© 2025 The Authors. Published by Elsevier Inc. This is an open access article under the CC BY license (<http://creativecommons.org/licenses/by/4.0/>).

Table 1

Main atmospheric properties of selected bodies in the solar system Venus: [Basilevsky and Head \(2003\)](#); Earth: [Saha \(2008\)](#); Mars: [Haberle \(2003\)](#); Titan: [Catling and Kasting \(2017\)](#) All compositions are given in mol %.

	Venus	Earth	Mars	Titan
Average atm. temperature	740 K	~ 293 K	200 K	93 K
Atm. pressure	93 bar	1 bar	6 mbar	1.5 bar
Atm. composition	96.5% CO <sub>2</sub> ,	78.09% N <sub>2</sub> ,	95.32% CO <sub>2</sub> ,	94.2% N <sub>2</sub>
	3.5% N <sub>2</sub>	20.95% O <sub>2</sub> ,	2.7% N <sub>2</sub> ,	5.6% CH <sub>4</sub>
	200 ppm SO <sub>2</sub>	0.93% Ar,	1.6% Ar	0.01% H <sub>2</sub>
		0.03% CO <sub>2</sub>	0.13% O <sub>2</sub>	

in exoplanetary systems ([Ronco and De Elfa, 2014](#); [Ronco et al., 2015](#); [Zain et al., 2018](#)).

Another process in the evolution of young terrestrial planets, which has an immense influence on the abundance and distribution of volatiles in planetary interiors is the magma ocean stage. When a planet experiences a giant impact with a magma ocean, it will lose a greater amount of its atmosphere due to increased surface motion compared to when the planet is only partially molten ([Genda and Abe, 2005](#)). Because volatiles are highly incompatible in most mantle minerals and will stay dissolved in the magma or degas if the magma is over-saturated, the presence of a magma ocean is conducive to a high heterogeneity of volatile constituents in the earliest solid mantle while also forming a thick early atmosphere ([Elkins-Tanton, 2012](#); [Hier-Majumder and Hirschmann, 2017](#)). [Hamano et al. \(2013\)](#) demonstrated that planets located within a critical distance to their host stars will keep their magma oceans for much longer periods of time (up to 100 Myrs) and, therefore, desiccate via hydrodynamic escape contrary to planets outside of the critical distance, which will solidify within several millions of years, retain their water, and do form primordial oceans.

Aside from uncertainties regarding the origins and initial compositions of rocky planets and moons, however, the evolution of their atmospheres remains unclear.

Venus's present-day atmosphere is a subject of debate, with conflicting theories about the atmosphere's geological recency ([Way and Del Genio, 2020](#)) or a fossilized state ([Odert et al., 2018](#)). Venus likely formed a thick H<sub>2</sub>O and CO<sub>2</sub> dominated atmosphere during the magma ocean stage ([Lichtenegger et al., 2016](#)). Some authors argue that Venus was unable to condense water during or after the magma ocean stage ([Gillmann et al., 2009](#); [Hamano et al., 2013](#)), while others believe there might have been an early wet, habitable phase, but likely evaporated its entire primordial ocean ([Kasting, 1988](#)). [Krissansen-Totton et al. \(2021\)](#) showed that both scenarios are possible assuming planetary evolution at mid-redox conditions. Regardless of which process formed the water steam atmosphere, it was exposed to efficient photodissociation into H and O followed by excessive H escape, thereby providing an explanation for the shifted D/H ratio ([Donahue et al., 1982](#)). Due to this excessive water loss, Venus may have become significantly desiccated ([Gillmann et al., 2009](#); [Hamano et al., 2013](#)). Alternatively, the high surface pressure might impede water degassing ([Gaillard and Scaillet, 2014](#)). However, current observations and models suggest that Venus has experienced marginal water degassing at least during its recent history ([Taylor and Grinspoon, 2009](#); [Noack et al., 2012](#); [Gillmann and Tackley, 2014](#)).

Mars, as indicated by SNC meteorites, acquired a rich supply of volatile elements during its formation ([Dreibus and Wänke, 1985](#)), but its current atmosphere is significantly depleted in C, N, and noble gases compared to Earth and Venus. Geochemical data and models suggest that much of the initial atmospheric inventory was removed prior to 3.7 Gyr by loss processes, including hydrogen escape and impact erosion. For the last 3.7 Gyr Mars has been predominantly dry and cold ([Carr and Head, 2010](#)). It is still under debate whether fluvial structures formed via ancient greenhouse effect enhanced by various gases impacts that created temporarily wet climates or periodic melting and saline brines with melting points much lower than 0 °C.

Titan with its cold N<sub>2</sub> and CH<sub>4</sub> atmosphere represents another extreme of atmospheric conditions and concentration ([Hörst, 2017](#)). The primary sources of nitrogen in Titan's atmosphere are most likely either N<sub>2</sub> or NH<sub>3</sub>, as suggested by [Strobel and Shemansky \(1982\)](#), which could have been incorporated during its formation or delivered afterward. If the initial nitrogen-bearing molecule was NH<sub>3</sub>, then subsequent processes such as photolysis ([Lewis, 1971](#); [Atreya et al., 1978](#)) or reactions within Titan's interior ([Glein et al., 2009](#); [Glein, 2015](#)) would be necessary for the present N<sub>2</sub> atmosphere. According to photochemical models, CH<sub>4</sub> in its current abundance would be destroyed by atmospheric chemistry within 30 Myr ([Yung et al., 1984](#); [Wilson and Atreya, 2004](#)). This suggests either a continuous or episodic resupply mechanism for CH<sub>4</sub> or that the atmosphere is not as old as the solar system. Models considering atmospheric escape and fractionation by chemistry, along with carbon isotope observations, indicate the possibility that either no significant fractionating loss process is occurring, the present methane is very recent, or the existence of a production/loss mechanism balancing escape over geological timescales ([Nixon et al., 2012](#); [Mandt et al., 2012](#)).

Earth is the only planet in the solar system that allows water to be present in all its states at its surface over longer periods of time. Earth's long-term climate stability is attributed to feedback involving atmospheric CO<sub>2</sub>, maintaining a warm climate even during the early times of the solar system when the Sun was less luminous. The removal of a substantial amount of CO<sub>2</sub> through crustal recycling during the Hadean era could have led to an atmosphere with approximately 1 bar of CO<sub>2</sub> and temperatures conducive to the formation of oceans (around 500 K, as suggested by [Zahnle et al. \(2015\)](#) and [Sleep et al. \(2014\)](#)). However, in contrast to [Sleep et al. \(2014\)](#), [Catling and Zahnle \(2020\)](#) argue that the early atmosphere might have been thin, with nitrogen (N<sub>2</sub>) constituting the primary atmospheric constituent at a partial pressure of around 0.3 bar, while the partial pressure of P<sub>CO<sub>2</sub></sub> ranged between 0.07 and 0.1 bar.

To enhance our understanding of how secondary atmospheres form and which key parameters they are influenced by, various authors have modeled volcanic degassing on a planetary scale. [Gaillard and Scaillet \(2014\)](#) tested the pressure effect of an existing atmosphere on degassing and showed that elevated surface pressures would result in dry volcanic gases abundant in N<sub>2</sub> and CO<sub>2</sub>, whereas lower pressure conditions favor the release of sulfur-rich gases. Intermediate atmospheric pressures, approaching 1 bar, would lead to volcanic emissions primarily composed of H<sub>2</sub>O. [Ortenzi et al. \(2020\)](#) demonstrated that mantle redox states influence atmospheric composition, thickness, and pressure, while planetary mass, thermal state, and age affect the degassing rate. [Woitke et al. \(2021\)](#) presented a method for the calculation of equilibrium chemistry at low temperatures, illustrating the compositional range that could emerge on cold planets (below 600 Kelvin). By varying the abundances of C, H, N, and O in the atmosphere, they categorized their findings into 4 groups. The rocky planets in our solar system serve as end-members of three of these types, with the exception of Earth, which exists in a state out of equilibrium as shown in [Fig. 1](#). [Liggins et al. \(2022\)](#) coupled their volcanic speciation model to an atmospheric equilibrium chemistry model and investigated the evolving atmospheres at surface temperatures ranging from 800 to 2000 K by varying mantle oxygen fugacity and defined three groups based on the most common gases. [Liggins et al. \(2023\)](#) added the kinetic effect of

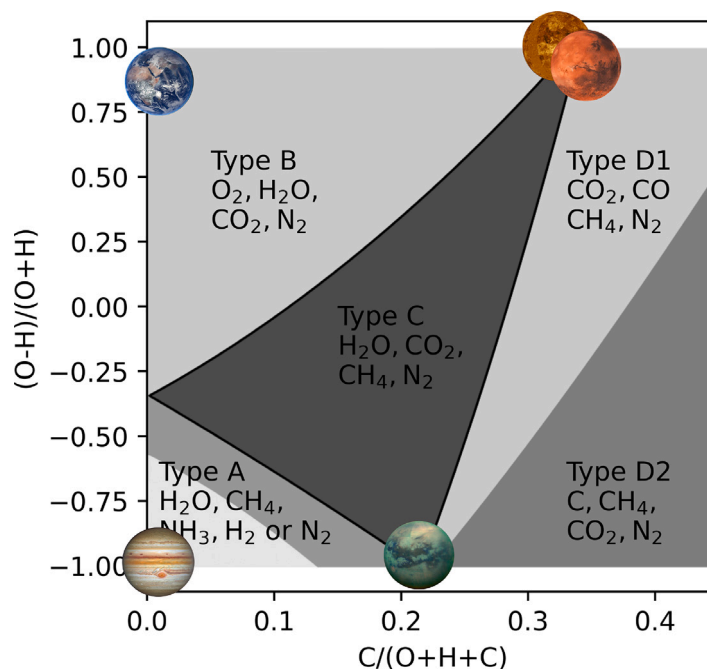


Fig. 1. Atmospheric types after [Woitke et al. \(2021\)](#) with examples from the solar system.

equilibrium reactions taking place, concluding that atmospheres below 700 K may never reach chemical equilibrium due to their kinetically limited slow reaction rates.

In our research, we coupled mantle melting, melt ascent, and volcanic degassing to an equilibrium chemistry model to better understand how cold (< 700 K) secondary atmospheres may have formed due to volcanic activity. We added water condensation and hydrogen escape to our model and investigated the effect the pressure of an accumulating degassed atmosphere would have on further degassing. Furthermore, we varied parameters such as melt production rates and extrusive output to demonstrate their influence on atmospheric chemistry. This indicates which atmospheric compositions may form abiotically and gives way to infer the bulk composition of planetary interiors based on their atmospheric chemistry evolving over time.

## 2. Methods

To understand what types of atmospheres can evolve from different planetary interiors, we have built a three-step model linking mantle to atmosphere composition through volcanic degassing. First, melt is produced in the mantle and its volatile content is set by the ambient pressure, temperature, initial volatile content of the mantle, degree of melting, and redox state. Secondly, volatile solubility, volcanic gas speciation and hence degassing are calculated with our speciation code. Lastly, the redistribution of gases in the atmosphere is modeled, incorporating processes such as water condensation, hydrogen escape, and the feedback effects of an existing atmosphere on further degassing. For most equilibrium chemistry calculations in the atmosphere, we used FastChem as described in [Stock et al. \(2022\)](#). To account for graphite precipitation and to compare results with [Woitke et al. \(2021\)](#), we employed FastChem Cond for specific runs. However, FastChem Cond was not applied universally due to its significantly longer computation time and the negligible impact of graphite precipitation on atmospheres not dominated by carbon (type A and type C atmospheres as seen in [Fig. 1](#)) (see [Table 2](#)).

### 2.1. Mantle melt partitioning - melt-solid-equilibrium

The oxygen fugacity of the mantle is set relative to the Iron Wustite buffer (IW) considering the pressure and temperature during mantle

Table 2

Physical properties set in the simulations unless stated otherwise in the results section, Earth was used as a model planet.

Physical property	Unit
Central star mass	$1.9885 \times 10^{24}$ kg
Stellar luminosity	$3.828 \times 10^{26}$ W
Star planet distance	1 AU
Mantle temperature	2000 K
Melt surface temperature	1400 K
Pressure at melting	10 GPa
Mantle mass	$4.01 \times 10^{24}$ kg
Planet radius	6371 km
Gravitational acceleration	$9.81 \text{ m s}^{-2}$
Initial atmospheric pressure	$10^{-8}$ bar

melt production. In most of our calculations, we presume an average surface melt flux of  $10^{14} \text{ kg yr}^{-1}$ , which corresponds to a scenario where the intrusive-to-extrusive ratio averages 10%, following the calculations of [Guimond et al. \(2021\)](#), who modeled melt production rates on a stagnant lid Archean Earth. To understand the influence of different melting fluxes and the resulting low- and high-pressure atmospheres on further atmospheric build-up, we vary the averaged surface melt production between  $10^{13} \text{ kg yr}^{-1}$  and  $10^{15}$ , thereby extending the lower and upper limits proposed by [Guimond et al. \(2021\)](#). To understand the influence of different melting fluxes and the resulting low- and high-pressure atmospheres on further atmospheric build-up, we vary the averaged surface melt production between  $10^{13} \text{ kg yr}^{-1}$  and  $10^{15}$ , thereby extending the lower and upper limits proposed by [Guimond et al. \(2021\)](#). These scenarios may arise not only from variations in the intrusive-to-extrusive ratio but also from differences in local melt fractions driven by variations in internal planetary heating. Since we do not model the early degassing history of a planet but examine the influence of melt production rate and surface flux, both parameters are held constant throughout each run. In the following, we define the H, N, and C content of the mantle, with a consideration for graphite saturation. To determine the H and N content of the melt, we employ the following equation

$$m_i^{melt} = \frac{m_i^{mantle}}{D_i + F(1 - D_i)} \quad (1)$$

where  $m_i^{melt}$  is the volatile content of each component in weight fraction,  $m_i^{mantle}$  is the volatile content of the bulk mantle,  $D_i$  is the partition coefficient and  $F$  is the average melt fraction, set to 0.1. We use the partition coefficient  $D_H = 0.01$  after (Katz et al., 2003; Aubaud et al., 2004). There is evidence that  $N$  partitioning is dependent on oxygen fugacity though experimental data for  $D_N$  is scarce. We interpolate linearly between the two values provided by Li et al. (2013) ( $5.53 \times 10^{-3}$  at IW and  $6 \times 10^{-4}$  at NNO, respectively). Carbon partitioning introduces additional complexity; we assume that in the mantle, carbon exists as graphite at oxygen fugacities below IW +3 and as carbonate at higher fugacities, partitioning into the melt in the form of carbonate ions ( $\text{CO}_3^{2-}$ ). Note that carbon may also dissolve as CO or CH<sub>4</sub> fluids as was recently shown by Gaillard et al. (2022), this effect was not included in our model but will be explored in future work. Carbonate partitioning is highly dependent on oxygen fugacity, we, therefore employ the equation described by (Holloway et al., 1992; Grott et al., 2011; Hirschmann and Withers, 2008) to calculate the carbon content of the melt:

$$m_{\text{CO}_3^{2-}}^{melt} = \frac{K_1 K_2 f_{\text{O}_2}}{1 - K_1 K_2 f_{\text{O}_2}} \quad (2)$$

with

$$\log_{10} K_1 = a - bT_{\text{mantle}} + cT_{\text{mantle}}^2 + d \frac{P_{\text{mantle}} - 1}{T_{\text{mantle}}} \quad (3)$$

$$\log_{10} K_2 = e - \frac{f}{T_{\text{mantle}}} - g \frac{P_{\text{mantle}} - 1000}{T_{\text{mantle}}} \quad (4)$$

where  $m_{\text{CO}_3^{2-}}^{melt}$  is the  $\text{CO}_3^{2-}$  content of the melt in weight fraction,  $a = 40.07639$ ,  $b = 2.53932 \times 10^{-2}$ ,  $c = 5.27096 \times 10^{-6}$ ,  $d = 0.0267$ ,  $e = -6.24763$ ,  $f = 282.56$ ,  $g = 0.119242$ ,  $T_{\text{mantle}}$  and  $P_{\text{mantle}}$  are the temperature and the pressure of the mantle in K and bar respectively, at the melting depth.

Assuming thermodynamic equilibrium, the weight fraction of  $\text{CO}_2$  of the melt can be calculated from  $m_{\text{CO}_3^{2-}}^{melt}$  with:

$$m_{\text{CO}_2}^{melt} = \left[ \frac{M_{\text{CO}_2}}{FWM} m_{\text{CO}_3^{2-}}^{melt} \right] / \left[ 1 - \left( 1 - \frac{M_{\text{CO}_2}}{FWM} \right) m_{\text{CO}_3^{2-}}^{melt} \right] \quad (5)$$

where  $M_{\text{CO}_2}$  is the molecular weight of  $\text{CO}_2$  and FWM is the formula weight of the melt normalized to oxygen, equal to  $36.594 \text{ g mol}^{-1}$  (Holloway et al., 1992; Grott et al., 2011).

Note that while Eqs. (2) to (4) do not directly encompass the concentration of the mantle source,  $m_{\text{CO}_2}^{melt}$  is constrained to the local source concentration. Knowing how much H, C, and  $N$  are dissolved in the melt, we can calculate equilibria between melt and gas (Section 2.2) and within the gas phase (Section 2.3) using our speciation code.

## 2.2. Solubility - melt-gas-equilibrium

While previous model studies focussing on volcanic outgassing considered only extrusive melt (e.g. Kite et al., 2009; Grott et al., 2011; Noack et al., 2017; Dorn et al., 2018; Ortenzi et al., 2020), Vulpius and Noack (2022) showed that intrusive outgassing even at greater depths may contribute considerable amounts to the overall degassed volatile budget of a planet due to fractional crystallization of the melt and subsequent oversaturation of incompatible volatiles. We do not consider intrusive volatile release but vary melt surface flux (and, therefore, extrusive output), leading to variations in the outgassing fluxes to take this effect into account. The solubility of volatiles in melts is highly dependent on the surrounding pressure. Since our model focuses exclusively on extrusive melt, the only pressure that needs to be accounted for is the pre-existing partial pressure of each component. To calculate this effect the following solubility law is used for the C-O-H species:

$$P_i^{surf} = \left( \frac{m_i^{melt}}{\alpha_i} \right)^{\beta_i} \quad (6)$$

where  $m_i^{melt}$  is the abundance in the melt of species  $i$ ,  $\alpha_i$  and  $\beta_i$  are Henrian fit coefficients shown in Table 3 and  $P_i^{surf}$  is the partial

**Table 3**

Henrian fit coefficients for each volatile species, to calculate their partial-pressure-dependent solubility, as described in Eq. (6). Data fitted by Lichtenberg et al. (2021) after:  $\text{H}_2\text{O}$ : (Silver et al., 1990); Holtz et al. (1995); Moore and Carmichael (1998); Yamashita (1999); Gardner et al. (1999); Liu et al. (2005);  $\text{H}_2$ : (Gaillard et al., 2003); Hirschmann (2012);  $\text{CO}_2$ : (Mysen et al., 1975); Stolper and Holloway (1988); Pan et al. (1991); Blank et al. (1993); Dixon et al. (1995);  $\text{CH}_4$ : (Ardia et al., 2013); Keppler and Golabek (2019);  $\text{CO}$ : (Yoshioka et al., 2019)

Molecule	$\alpha$ (ppm/Pa)	$\beta$ (nondim.)
$\text{H}_2\text{O}$	1.033	1.747
$\text{H}_2$	$2.572 \times 10^{-6}$	1.000
$\text{CO}_2$	$1.937 \times 10^{-9}$	0.714
$\text{CO}$	$1.600 \times 10^{-7}$	1.000
$\text{CH}_4$	$9.937 \times 10^{-8}$	1.000

pressure of species  $i$  at the surface, which is calculated here in Pa and needs to be converted to bar.

The treatment of nitrogen solubility is more complex: the physical dissolution of nitrogen, which occurs mainly in oxidized magmas can be described by a Henry's Law behavior, here Nitrogen occurs as  $\text{N}_2$  molecules. In reduced magmas, however, nitrogen dissolves as an  $N$  radical and is chemically bound to the silicate network, resulting in its solubility being several orders of magnitude higher. To incorporate this effect in our calculations we use the solubility law by Libourel et al. (2003):

$$[N] = 0.0611 * P_{\text{N}_2} + f_{\text{O}_2}^{-3/4} * 5.97 * 10^{-10} * P_{\text{N}_2}^{1/2} \text{ for } f_{\text{O}_2} < \text{IW} -1.3 \quad (7)$$

$$[\text{N}_2] = 2.21 * 10^{-9} * P_{\text{N}_2} + f_{\text{O}_2}^{-3/4} * 2.13 * 10^{-17} * P_{\text{N}_2}^{1/2} \text{ for } f_{\text{O}_2} > \text{IW} -1.3 \quad (8)$$

Note that the experiments carried out to formulate this solubility law were carried out in an H-free system at 1 bar and therefore ignore the possible stability of NHx complexes.

## 2.3. Speciation - gas-gas-equilibrium

Knowing the amount of each volatile partitioning into the melt and being dissolved, we can calculate how much gas will be formed. However, since Eqs. (1) to (7) employ weight fractions, while Eq. (8) and the speciation are determined in mole fractions, it is necessary to perform a conversion, which can be calculated with:

$$X_i = \frac{m_i \text{MMW}}{M_i} \quad (9)$$

where  $X_i$  is the mole fraction,  $m_i$  the weight fraction, and  $M_i$  is the molecular weight of species  $i$ , and MMW denotes the mean molecular weight of the mixture. Speciation can now be calculated using the simple mass balance equation:

$$X_i^{total} = X_i^{melt} + X_i^{gas} \quad (10)$$

The volatile species in the gas phase will then speciate into molecules depending on oxygen fugacity, temperature, and pressure. The relevant reactions in the C-H-O-N system are:



The corresponding equilibrium constants of these reactions are:

$$K_1 = \frac{f_{\text{H}_2} f_{\text{O}_2}^{0.5}}{f_{\text{H}_2\text{O}}} \quad (11)$$

$$K_2 = \frac{f_{\text{CO}} f_{\text{O}_2}^{0.5}}{f_{\text{CO}_2}} \quad (12)$$

$$K_3 = \frac{f_{\text{CH}_4} f_{\text{O}_2}^2}{f_{\text{CO}_2} f_{\text{H}_2\text{O}}^2} \quad (13)$$

$$K_4 = \frac{f_{\text{NH}_3}^2 f_{\text{O}_2}^{1.5}}{f_{\text{N}_2} f_{\text{H}_2\text{O}}^3} \quad (14)$$

The fugacity ( $f_i$ ) of each phase can be expressed by the equation:

$$f_i = X_i \gamma_i P \quad (15)$$

where  $X_i$  is the mole fraction,  $\gamma_i$  is the fugacity coefficient of each phase and  $P$  is the surrounding pressure. Assuming an ideal behavior of the gases ( $\gamma_i = 1$ ), the equations for the equilibrium constants can be rewritten as:

$$K_1 = \frac{X_{\text{H}_2} f_{\text{O}_2}^{0.5}}{X_{\text{H}_2\text{O}}} \quad (16)$$

$$K_2 = \frac{X_{\text{CO}} f_{\text{O}_2}^{0.5}}{X_{\text{CO}_2}} \quad (17)$$

$$K_3 = \frac{X_{\text{CH}_4} f_{\text{O}_2}^2}{X_{\text{CO}_2} X_{\text{H}_2\text{O}}^2 P^2} \quad (18)$$

$$K_4 = \frac{X_{\text{NH}_3}^2 f_{\text{O}_2}^{1.5}}{X_{\text{N}_2} X_{\text{H}_2\text{O}}^3 P^2} \quad (19)$$

We calculate the equilibrium constants using the NASA thermodynamic database (Burcat et al., 2005). We assume that the oxygen fugacity of the gas is equal to the oxygen fugacity of the magma and hence the mantle.

We set the temperature of the magma and hence degassing to 1400 K and calculate the oxygen fugacity and the equilibrium constants accordingly. The pressure is determined by the pressure of the atmosphere which is set to  $10^{-8}$  bar in the beginning and then updated after each degassing step. With a given temperature, pressure, and oxygen fugacity, the speciation can be solved numerically. To account for mantle depletion, the degassed mass of each species is removed from the mantle budget. The atmospheric pressure can then be calculated according to:

$$P_{\text{atm}} = \frac{M_{\text{atm}} g}{A_p} \quad (20)$$

Where  $P_{\text{atm}}$  is the atmospheric pressure in Pa,  $M_{\text{atm}}$  is the atmospheric mass,  $g$  is the gravitational acceleration at the surface and  $A_p$  is the surface area of the planet.

After magma degassing we calculate water condensation since it is expected to be much faster than equilibrium chemistry at low atmospheric temperatures (Liggins et al., 2023). We calculate water condensation after (Saul and Wagner, 1987) via:

$$\ln\left(\frac{P_{\text{H}_2\text{O}}}{P_c}\right) = \frac{T_c}{T_{\text{atm}}} \left[ a_1 \tau + a_2 \tau^{1.5} + a_3 \tau^3 + a_4 \tau^{3.5} + a_5 \tau^4 + a_6 \tau^{7.5} \right] \quad (21)$$

with  $P_c = 220.64$  bar,  $T_c = 647.096$  K,  $\tau = \frac{T}{T_c}$ ,  $a_1 = -7.85951783$ ,  $a_2 = 1.84408259$ ,  $a_3 = -11.7866497$ ,  $a_4 = 22.6807411$ ,  $a_5 = -15.9618719$ ,  $a_6 = 1.80122502$  Using Eq. (21), we can calculate both the amount of water vapor that remains in the atmosphere and the amount of water that condenses. This enables us to determine the equivalent global layer thickness, a hypothetical value representing the potential thickness of an oceanic layer, assuming all condensed water stays on the surface.

## 2.4. Atmospheric composition

To calculate the atmospheric redistribution of all species under surface conditions we use FastChem as described in Stock et al. (2022). By executing the steps described in Sections 2.1–2.3 the model provides the essential input parameters for FastChem such as atmospheric

pressure and volatile abundances. Surface temperature is influenced by several processes, including the distance to the star and other bodies (tidal heating), radiogenic heating from the planet's interior, tectonic regime, and atmospheric composition and thickness. To explore its effect on atmospheric composition across a wide parameter range, the surface temperature is varied rather than being dynamically calculated, as this would require a sophisticated climate evolution model. Subsequently, FastChem undertakes comprehensive atmospheric chemistry calculations, considering all 85 chemical species within its scope. This approach may yield results extending beyond the species initially considered in our speciation code, encompassing reactions R1 to R4. Despite the sophisticated reequilibration by Fastchem, using our speciation code and its chemical equilibrium is necessary as it incorporates the equilibrium between atmospheric abundance and solubility in the melt of any given species and calculates the speciation dependent on melt oxygen fugacity. Following this re-equilibration phase, we proceed to assess various atmospheric processes, including  $\text{H}_2$  escape and graphite precipitation, all of which have significant implications for the atmospheric composition.

### 2.4.1. Hydrogen escape

Given hydrogen's high susceptibility to mass-dependent thermal atmospheric loss as compared to other gases in our calculation, we employ the hydrogen escape modeling approach outlined in Baumeister et al. (2023), to ensure a more precise depiction of atmospheric evolution. We distinguish between two distinct loss mechanisms: energy-limited loss for atmospheres primarily composed of hydrogen (with a molar fraction of  $\text{H}_2 > 20\%$ ) and diffusion-limited loss for atmospheres dominated by other species (with a molar fraction of  $\text{H}_2 < 10\%$ ). Energy-limited loss is contingent upon the extent of XUV radiation absorbed by the atmosphere and can be computed using the formula:

$$M_{el} = \frac{\epsilon \pi R_p^2 R_{\text{atm}}^2 F_{\text{XUV}}}{GM_p} \quad (22)$$

Here,  $\epsilon$  represents an efficiency factor set to 0.15 based on Kite and Barnett (2020),  $R_p$  denotes the planet's radius,  $R_{\text{atm}}$  signifies the radius of the planet at the top of the atmosphere (defined at 10 mbar)  $G$  is the gravitational constant, and  $M_p$  denotes the planet's mass.

On the other hand, diffusion-limited loss hinges on the upward mixing and diffusion of  $\text{H}_2$  through the upper atmosphere and can be expressed as follows:

$$M_{dl} = 4\pi R_{\text{atm}}^2 \frac{m_{\text{H}_2}}{N_A} b_{aj} X_{\text{H}_2} \left( \frac{1}{H_a} - \frac{1}{H_{\text{H}_2}} \right) \quad (23)$$

where  $m_{\text{H}_2}$  denotes the molecular weight of  $\text{H}_2$ ,  $N_A$  is the Avogadro constant,  $b_{aj}$  represents the diffusion coefficient between  $\text{H}_2$  and each background gas,  $X_{\text{H}_2}$  denotes the molar fraction of  $\text{H}_2$  in the atmosphere, and  $H_a$  and  $H_{\text{H}_2}$  are the unperturbed scale heights of the background gas and  $\text{H}_2$  respectively.

Note that Eq. (22) and Eq. (23) should be regarded as upper limits for escape rates, providing an estimate of the maximum possible rates. Much about escape rates remains poorly understood, especially in mixed atmospheres (Johnstone et al., 2018). The equations used here are commonly applied in exoplanet studies (e.g. Katyal et al., 2020; Kite and Barnett, 2020).

After establishing the new atmospheric conditions, we adjust the atmospheric pressure and chemical abundances to account for the effects of the preceding steps. The revised partial pressure of each gas will affect its solubility and consequently the degassing process in subsequent steps. This iterative process is repeated 100 times, simulating atmospheric buildup over a period of 1 Gyr, using smaller timesteps did not influence the results significantly.

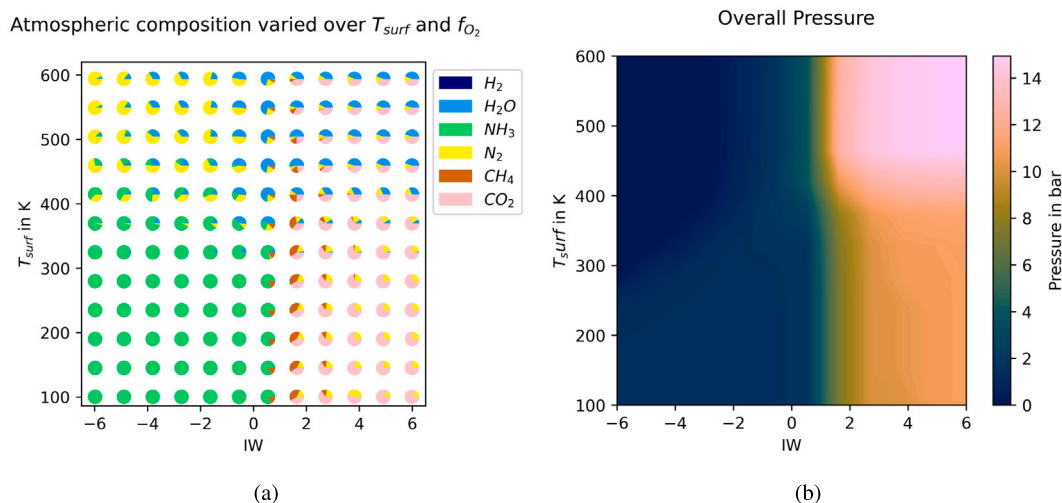


**Fig. 2.** Atmospheric composition varied over  $T_{surf}$  and oxygen fugacity visualized as pie charts (a) and the respective atmospheric pressure (b). Melt surface flux was held constant at  $10^{14} \text{ kg yr}^{-1}$ , volatile content of the mantle was set to values expected for Earth after the Magma Ocean stage: 450 ppm  $\text{H}_2\text{O}$ , 50 ppm  $\text{CO}_2$ , 10 ppm N.

**Table 4**

Estimated oxygen fugacity of terrestrial bodies in the solar system relative to the Iron-Wustite buffer. References: (1) [McCubbin et al. \(2012\)](#), (2) [Nicklas et al. \(2019\)](#) (3) [Frost and McCammon \(2008\)](#), (4) [Wadhwa \(2008\)](#).

Body	$f_{\text{O}_2}$ related to Iron Wustite buffer	reference
Mercury	-6.3 to -2.6	1
Venus	Primitive mantle: +0	2
Earth	MORB: +4	3
	Spinel peridotite: +2 to +6 Lower mantle: -1.5 to 0	3
Moon	-2 to 0	4
Mars	basaltic shergottites: 0 to +2	4
	nakhilites: +3 to +4	4

### 3. Results

In our study, we conducted a comprehensive series of simulations and explored the effect key parameters such as mantle oxygen fugacity (Section 3.1), surface temperature and melt production rates (Section 3.2), and volatile abundance in the mantle (Section 3.3) have on atmospheric composition and atmospheric pressure. We first investigated the possible C-H-O-N atmospheric parameter space that can be explained by pure volcanic outgassing (e.g. in the absence of life or cometary infall). For this purpose and to put our resulting atmospheres into a more general context, we followed the categorization proposed by [Woitke et al. \(2021\)](#) and classified the resulting atmospheric compositions into three primary types (A, B, C). Interestingly, in certain simulations a fourth atmospheric type (D) emerged, characterized by the presence of  $\text{CO}_2$ ,  $\text{CH}_4$ ,  $\text{CO}$ , and  $\text{N}_2$ . Type D atmospheres were characterized by [Woitke et al. \(2021\)](#) but were considered to be unstable due to the instability of  $\text{CO}$  and the extensive condensation of graphite (further discussed in Section 3.3).

#### 3.1. Oxygen fugacity

Of all varied parameters mantle oxygen fugacity has the strongest influence on emerging atmospheric composition and pressure. We varied oxygen fugacity from IW -6 to IW +6 based on values observed in the solar system as shown in [Table 4](#).

Terrestrial mantles with low oxygen fugacities between IW -6 and IW +0 produce thin H- and N-dominated Type A atmospheres with atmospheric pressures ranging from 1.2 mbar at low to 2 bar at high melt production rates. At low temperatures around 300 K these atmospheres

are  $\text{NH}_3$  dominated ([Fig. 3\(a\)](#)), while at higher temperatures (600 K)  $\text{N}_2$  and  $\text{H}_2\text{O}$  occur ([Fig. 3\(b\)](#)).  $\text{H}_2$  is excessively degassed but generally escapes except for some special cases with high melt production (Section 3.2). In these cases more than four gases are present at 600 K, meaning that the model by [Woitke et al. \(2021\)](#) is not applicable anymore. Carbon is barely present at reduced conditions because of its highly  $f_{\text{O}_2}$  dependent solid melt partitioning. At intermediate mantle oxygen fugacities ranging from IW +0 to IW +2, carbon appears as  $\text{CH}_4$  at more reduced and as  $\text{CO}_2$  at oxidized conditions, hence we observe a switch from type A to type C atmospheres at IW +2. At surface temperatures of 300 K,  $\text{CH}_4$  and  $\text{CO}_2$  surpass  $\text{NH}_3$  as the dominant atmospheric species, at 600 K  $\text{H}_2\text{O}$  predominates unless there is substantial high melt production exceeding  $10^{14} \text{ kg yr}^{-1}$  in which case  $\text{CO}_2$  exhibits higher partial pressures. The appearance of carbon in the atmosphere results in a significant increase in atmospheric pressure shown in [Fig. 3](#). Conversely, to reduced conditions, mantles with high oxygen fugacities ranging from IW +2 to IW +6 produce thick  $\text{CO}_2$ -dominated type C atmospheres with  $\text{N}_2$ ,  $\text{CH}_4$  and  $\text{H}_2\text{O}$  at higher temperatures. Atmospheric pressure in these cases range from 3 bar to 80 bar. Type B atmospheres were never observed in any of our simulations since oxygen degassing is always bound to either  $\text{H}_2\text{O}$  or  $\text{CO}_2$ , resulting in sufficient amounts of carbon and hydrogen to never form  $\text{O}_2$  via equilibrium chemistry. The atmospheric evolution over a 1 Gyr period for several selected runs is depicted in [Figs. 5 to 9](#) in the Appendix.

#### 3.2. Surface temperature and melt production rates

We varied surface temperature between 100 K and 600 K to explore its effect on the planet's atmosphere as shown in [Fig. 2\(a\)](#). Low atmospheric temperatures will favor  $\text{NH}_3$  dominated (type A) atmospheres at reduced and  $\text{CO}_2$  dominated (type C) atmospheres with  $\text{CH}_4$  and  $\text{N}_2$  as secondary gases at oxidized conditions. Water is generally lost from the atmosphere due to condensation at these temperatures. Conversely, at 600 K water is abundant across a wide range of parameters and is the dominant atmospheric species at low degassing rates (Section 3.2).  $\text{NH}_3$  is only abundant in small amounts, as higher surface temperatures favor a mixture of  $\text{N}_2$  and  $\text{H}_2$ , which is generally lost. The surface temperature exerts an influence on atmospheric pressures, albeit relatively minor when compared to the influence of melt production as detailed in [Fig. 2\(b\)](#). In type A atmospheres (low oxygen fugacities) colder atmospheres are slightly denser because the formation of  $\text{NH}_3$  leads to lower hydrogen loss rates. Furthermore, following the solubility law by [Libourel et al. \(2003\)](#),  $P_{\text{N}_2}$  mitigates further degassing, unlike

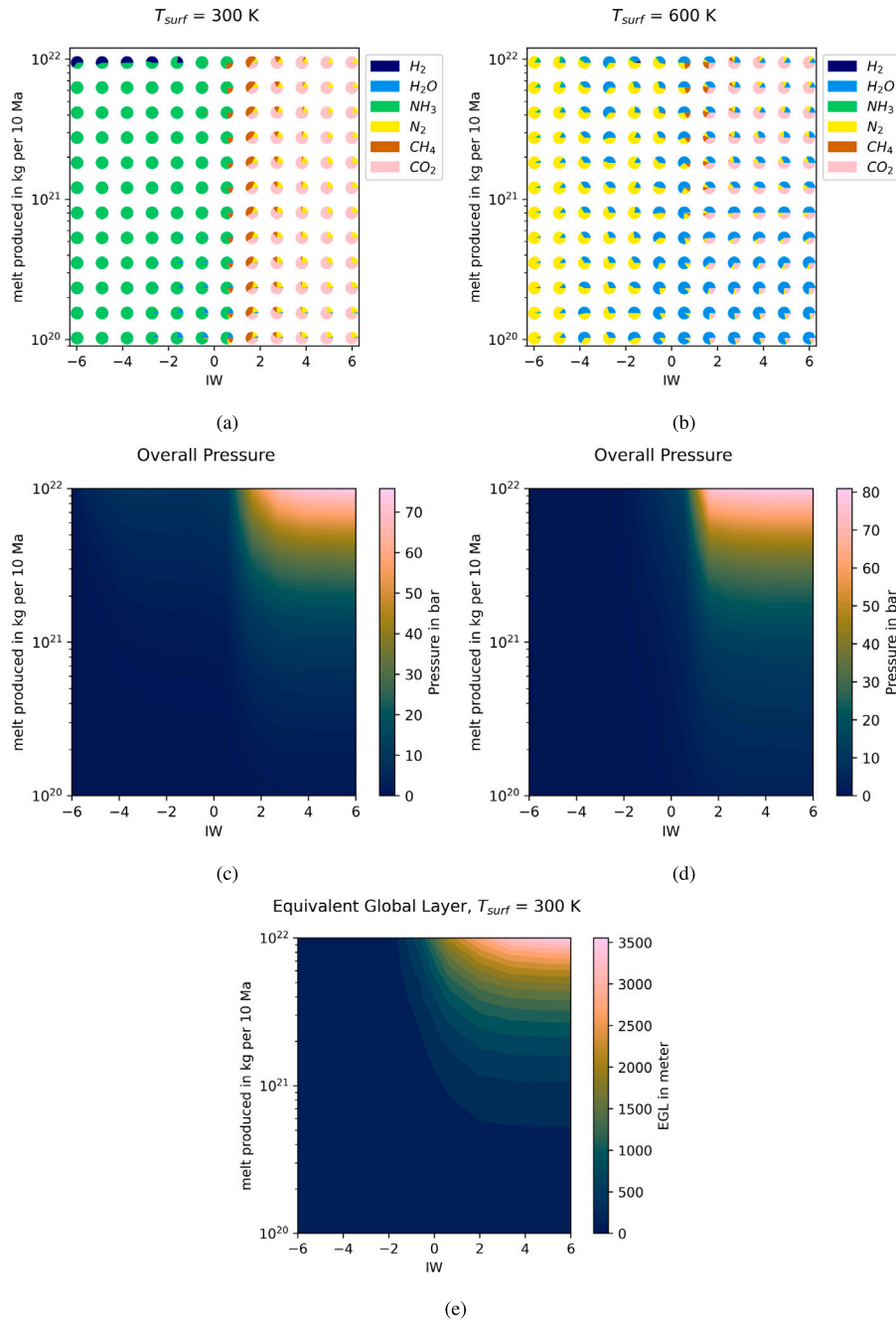


**Fig. 3.** Atmospheric composition visualized as pie charts at different melt production rates and mantle oxygen fugacities at 300 K (a) and 600 K (b) surface temperature and their respective surface pressures (c) and (d). (E) shows the respective equivalent global layer at 300 K. Volatile content of the mantle was set to values expected for Earth after the Magma Ocean stage: 450 ppm  $H_2O$ , 50 ppm  $CO_2$ , and 10 ppm N.

$P_{NH_3}$ , which contributes to higher rates of nitrogen degassing. In type C atmospheres, this trend is reversed, as water remains in vaporized form at high temperatures, resulting in slightly elevated surface pressures.

Melt surface fluxes on an Earth-sized planet were varied between  $10^{13}$   $kg\ yr^{-1}$  and  $10^{15}$   $kg\ yr^{-1}$  and were fitted to smaller and larger planets accordingly. As expected, the melt flux exerts a significant influence on atmospheric pressure, particularly amplifying pressures in the presence of higher melt outputs, especially under conditions of elevated oxygen fugacities as shown in Figs. 3(c) and 3(d). Moreover, it profoundly impacts the atmospheric composition and the rainout of water and hence the formation of oceans.

### 3.2.1. 300 Kelvin

The atmospheric composition after 1 billion years at varied melt surface flux and oxygen fugacity at a surface temperature of 300 K is detailed in Fig. 3(a). The atmospheric pressure in this scenario ranges between 1.5 mbar and 75 bar (Fig. 3(c)). While the surface melt flux exerts minimal influence on which gas phase dominates, it significantly affects the abundance of the gases present. Specifically, higher surface melt fluxes increase the abundance of  $CO_2$ ,  $CH_4$ ,  $NH_3$ , and  $H_2$ . Conversely, lower melt fluxes lead to higher prominence of  $H_2O$  and  $N_2$ .  $H_2$  generally escapes the atmosphere unless surface melt fluxes are extremely high and oxygen fugacity is low. In such cases, hydrogen degassing surpasses energy-limited hydrogen escape fluxes,

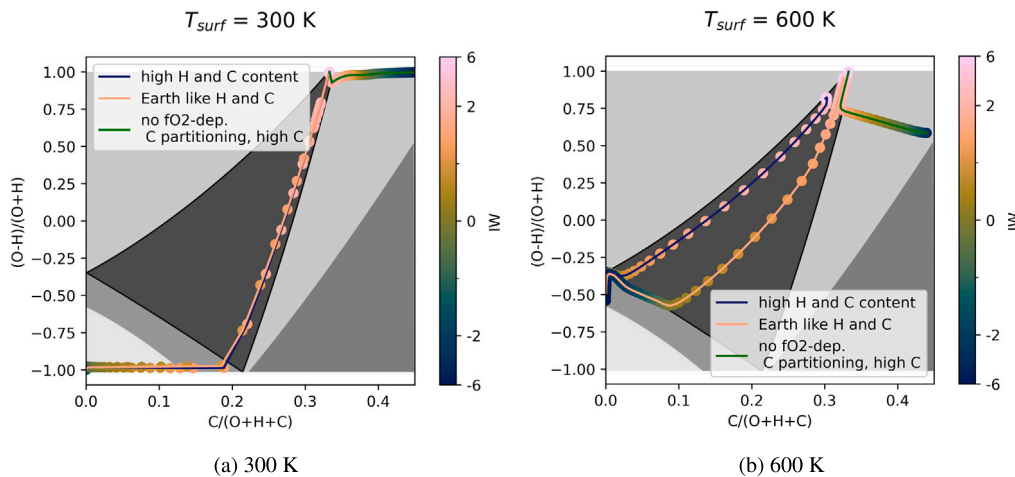


Fig. 4. Atmospheric composition at different mantle oxygen fugacities and volatile inventories plotted in the Woitke Diagram (Fig. 1) at a surface temperature of a) 300 and b) 600 K. Each dot represents the atmospheric composition after 1 Gyr dependent on the mantle oxygen fugacity. The colored lines represent different initial volatile inventories: orange line: earth-like mantle composition after the magma ocean stage according to Elkins-Tanton (2008) with 450 ppm H<sub>2</sub>O and 50 ppm CO<sub>2</sub>, blue line: enriched mantle with 700 ppm H<sub>2</sub>O and 700 ppm CO<sub>2</sub>, green line: oxygen-fugacity-dependent carbonate partitioning ignored, mantle with 100 ppm H<sub>2</sub>O and 500 ppm CO<sub>2</sub>. Melt surface flux was held constant at 14 kg yr<sup>-1</sup>.

allowing it to persist in the atmosphere, as detailed in Section 4.3. Furthermore, melt production rates significantly influence liquid water formation at low atmospheric temperatures, as shown in Fig. 3(e). Depending on these rates, an equivalent global water layer ranging from 0 to 3500 meters was observed, which has substantial implications for other planetary processes.

### 3.2.2. 600 Kelvin

The atmospheric composition after 1 billion years at varied melt surface flux and oxygen fugacity at a surface temperature of 600 Kelvin is illustrated in Fig. 3(b). The atmospheric pressure in this scenario ranges between 1.2 mbar and 81 bar, which is slightly higher than at 300 Kelvin due to the remaining water in the atmosphere. Unlike the scenario at lower temperatures, at 600 Kelvin, the surface melt flux significantly influences both the abundance and the dominance of the atmospheric gases.

At mantle oxygen fugacities below IW -1, N<sub>2</sub> or H<sub>2</sub>O are the dominant species. The primary of these two gases is determined by three competing processes: the pressure-dependent solubility of water in the melt, the oxygen fugacity-dependent speciation from H<sub>2</sub> to H<sub>2</sub>O, and the pressure and oxygen fugacity-dependent solubility of nitrogen in the melt. Additionally, at high melt surface fluxes, small amounts of NH<sub>3</sub> and H<sub>2</sub> remain stable in the atmosphere.

When the mantle oxygen fugacity is higher than IW -1, H<sub>2</sub>O or CO<sub>2</sub> dominate the atmosphere, with water being the dominant species at lower melt surface fluxes. This is because water degassing remains largely unbuffered under reduced atmospheric pressures. Additionally, at high surface melt fluxes, methane (CH<sub>4</sub>) is stable for mantle oxygen fugacities between IW +0 and IW +2.

### 3.3. Volatile abundance

Volatile abundances of hydrogen, carbon, and nitrogen were varied to accommodate various volatile delivery and building block scenarios. The variations that were tested are H: 100 - 700 ppm, C: 50 - 700 ppm, N: 10 - 100 ppm. Despite these adjustments, while the volatile abundances influenced atmospheric pressures and the abundance of corresponding gas species, there was minimal impact on atmospheric classifications. The general observation that degassing from reduced mantles produced type A atmospheres and oxidized mantles produced type C atmospheres remained unchanged. Type B atmospheres were never produced despite numerous runs with different initial volatile

inventories. A selection of these runs is shown in Fig. 4. Note that nitrogen abundances were not varied in Fig. 4, as the results here are plotted as a function of C/(H + O + C) and (O-H)/(O + H) following the classification of Woitke et al. (2021), and because nitrogen does not notably affect the H-C-O system. This decoupling between initial volatile inventory and atmospheric composition can be explained by carbon abundances being primarily controlled by redox melting, while water abundance is influenced by melt oxygen fugacity and condensation. Furthermore, Woitke et al. (2021) observed significant graphite precipitation in their results using the equilibrium chemistry code GGChem. They concluded that this process rendered type C atmospheres, particularly those near the type D boundary, highly improbable, favoring a shift toward type B atmospheres instead (as illustrated in their Fig. 2). In contrast, our simulations did not replicate this effect across the tested parameter ranges. Although graphite condensation occurred in our models, its influence was minimal, and carbon predominantly remained in the form of CO<sub>2</sub> or CH<sub>4</sub>.

The only noteworthy deviation of type A and C atmospheres occurred when carbon was enriched and hydrogen depleted and the effects of  $f_{O_2}$ -dependent carbon melt-solid partitioning were ignored. In these cases, the concentration of carbon in the mantle was set between 500 and 700 ppm and the concentration in the melt was calculated using Eq. (1) for all mantle oxygen fugacities. Under these conditions, a third atmospheric type emerged, characterized by the dominance of CO<sub>2</sub> alongside significant levels of CO, CH<sub>4</sub>, and N<sub>2</sub>, which is shown in Fig. 4. As mentioned earlier, this atmospheric type was described by Woitke et al. (2021), but was considered improbable due to the instability of CO at low atmospheric temperatures and the extensive condensation of graphite, as further detailed by Moses et al. (2013). To investigate this, we utilized Fastchem and Fastchem Cond across varying atmospheric temperatures and average melt surface fluxes ( $1 \times 10^{14}$  kg yr<sup>-1</sup>), yielding the following results: Fastchem calculations revealed the coexistence of CO<sub>2</sub>, CO, and CH<sub>4</sub> over the tested temperature range (300 K to 600 K), with CO becoming more dominant above 500 K and CO<sub>2</sub> dominating below this threshold, at an overall atmospheric pressure of 70 bar, as shown in Fig. 8 in the Appendix. In contrast, Fastchem Cond simulations showed that at 300 K, CO and CH<sub>4</sub> were eliminated due to substantial graphite precipitation, resulting in a CO<sub>2</sub>-dominated atmosphere (65 bar), as presented in Fig. 9 in the Appendix. Consequently, at 300 K, a type D atmosphere is unlikely and instead transitions to a type C atmosphere, positioned in the upper corner of the gray triangle depicted in Fig. 4. Above 400 K, our results diverge significantly from those of Woitke et al. (2021), as CO and



CH<sub>4</sub> remain stable. While graphite precipitation occurs at these higher temperatures, it does not markedly affect the outcomes compared to those obtained without accounting for graphite condensation.

#### 4. Discussion

Our research delves into the formation of secondary atmospheres through volcanic degassing on diverse planetary bodies, with a focus on varying crucial parameters such as mantle composition, oxygen fugacity, surface temperature, and planet size.

In our modeling approach, we take into account several pivotal processes in the formation of a secondary atmosphere on an abiotic planet, notably volcanic degassing, thermodynamic re-equilibration, atmospheric hydrogen escape, and water condensation. However, it is crucial to acknowledge that there are various other significant processes that we do not incorporate into our model. These include non-volcanic degassing, photochemistry, the effects of impact erosion, transformation, and volatile delivery and biological processes. No initial atmosphere is assumed in the model, but magma ocean degassing may have already produced a thick atmosphere, e.g. owing to substantial NH<sub>3</sub> degassing during the Archean period, as proposed by Li et al. (2013). Furthermore, our simplification of setting a general surface temperature for a planet proves to be an oversimplification, as surface temperature is influenced by a myriad of factors, encompassing distance from the sun, albedo, conduction within the planet's interior, and the presence of greenhouse gases. Additionally, temperature distribution across a planet's surface is far from uniform, with atmospheres exhibiting different layers with distinct properties, and tidally locked planets experiencing extreme temperature variations between their frigid night sides and scorching day sides. The formation of clouds further complicates matters, altering various physical properties, including albedo, in intricate ways. Another key parameter, which treatment is overly simplified in our model, is oxygen fugacity. It has become common practice in magma degassing models to assign oxygen fugacity as a universal variable, adjusted based on the specific redox conditions being considered (either reduced or oxidized). However, in reality, the oxygen fugacity ( $f_{O_2}$ ) is determined by the equilibrium between ferrous and ferric iron oxides within the silicate melt, thus potentially fluctuating over time or with depth (e.g. Deng et al., 2020). Furthermore, some authors argue that the kinetic effects of the reactions taking place at cold atmospheric temperatures, especially the formation of CH<sub>4</sub> and NH<sub>3</sub>, significantly decelerate these reactions to the extent that time scales beyond those considered in this paper are reached (e.g. Liggins et al., 2023). We do not consider these effects and assume that an equilibrium is reached within the considered time of each step (10 Myrs). However, over longer timescales, it is conceivable that mixtures of the atmospheric types described here, along with additional compounds might emerge. For instance, gases commonly degassed in our model include H<sub>2</sub>O, H<sub>2</sub>, CO, CO<sub>2</sub>, and N<sub>2</sub>. While CO is typically unstable and vanishes from the atmosphere after equilibrium chemistry is applied, CH<sub>4</sub> and NH<sub>3</sub> are primarily produced in significant amounts only under equilibrium conditions at low surface temperatures. Incorporating kinetic effects could enable the coexistence of species such as CO and CH<sub>4</sub>, or NH<sub>3</sub> and N<sub>2</sub> in type A atmospheres, as well as CO<sub>2</sub> and CO in type C atmospheres.

##### 4.1. Dominant atmospheric types

Primarily, it is seen that atmospheres with surface temperatures below 700 K tend to fall into two primary categories. Reduced mantles predominantly would result in Type A atmospheres characterized by the presence of H<sub>2</sub>, H<sub>2</sub>O, CH<sub>4</sub>, NH<sub>3</sub>, and N<sub>2</sub>. In contrast, Type C atmospheres, marked by the prevalence of CO<sub>2</sub>, H<sub>2</sub>O, N<sub>2</sub>, and CH<sub>4</sub>, will emerge at higher oxygen fugacities (IW +0 to IW +6). An interesting revelation is the potential stability of atmospheres composed of CO<sub>2</sub>, CO, CH<sub>4</sub>, and N<sub>2</sub> under specific conditions where hydrogen is scarce,

thereby suggesting unique atmospheric compositions. Furthermore, our results indicated that while H<sub>2</sub>O was more abundant in the planetary mantle, its presence in the atmosphere remained generally lower than that of CO<sub>2</sub> unless melt surface fluxes were low. This discrepancy was attributed to the higher solubility of water in the melt, with variations in solubility laws producing divergent outcomes. Additionally, our study demonstrated that type B atmospheres were not produced through volcanic degassing, even with super-oxidized magmas. This is because oxygen always degassed as H<sub>2</sub>O, CO<sub>2</sub>, or CO, ensuring there is enough H or C to form H<sub>2</sub>O or CO<sub>2</sub> in the atmosphere, making O<sub>2</sub> thermodynamically unfavorable.

Nonetheless, some authors have shown two possibilities for abiotic O<sub>2</sub> formation. Gaillard et al. (2021) proposed the degassing of trace amounts of O<sub>2</sub> under super-oxidized conditions in Fe-rich, S-poor magmas. Luger and Barnes (2015) suggest that planets orbiting M dwarf stars might develop abiotic O<sub>2</sub> atmospheres during the magma ocean stage, driven by the formation of thick water steam atmospheres and the photolysis of water vapor and subsequent hydrogen escape. This process would lead to complete surface desiccation as it has been proposed for Venus (e.g. Kulikov et al., 2006; Gillmann et al., 2009). However, to completely eradicate the entire water budget of a planet it would need extremely sufficient solar radiation in the absence of O<sub>2</sub> sinks. Furthermore, the stability of such high O<sub>2</sub> concentrations remains uncertain due to the combustibility of O<sub>2</sub> (Grenfell et al., 2018).

In summary, while abiotically formed O<sub>2</sub> is theoretically possible, it appears to be relatively rare, and thus, O<sub>2</sub> may still be considered a potential biosignature. As pointed out by Woitke et al. (2021) and contrary to Krissansen-Totton et al. (2018) or Thompson et al. (2022), the combination of CH<sub>4</sub> and CO<sub>2</sub> does not serve as a reliable biosignature around G type stars, as both gases commonly coexist in our simulations.

##### 4.2. Implications for the solar system

The oxidation state of Venus's mantle remains uncertain, with estimates generally predicting values around or slightly above the Iron-Wüstite buffer. Additionally, little is known about the volatile budget of Venus. In our study, we adopted a volatile budget similar to that estimated for Earth after magma ocean (MO) solidification, with 450 ppm H<sub>2</sub>O, 50 ppm CO<sub>2</sub> (as per Elkins-Tanton, 2008), and set nitrogen to 10 ppm while varying oxygen fugacity from IW +0 to IW +2, while assuming surface temperatures as observed today. Our model indicates that the melt surface flux must have been quite high to reach the elevated surface pressures observed today on Venus. Varying the oxygen fugacity between IW +0 and IW +2 significantly influences the results. At IW +0, the atmospheric pressures after are  $P_{CO_2}$  0.0015 bar,  $P_{CH_4}$  0.89 bar,  $P_{H_2O}$  2.9 bar,  $P_{N_2}$  4.1 bar, leading to an overall atmospheric pressure of 7.8915 bar after 1 Gyrs. In contrast, at IW +2, the pressures are  $P_{CO_2}$  38.3 bar,  $P_{CH_4}$  7.4 bar,  $P_{H_2O}$  11.9 bar,  $P_{N_2}$  7.5 bar, with an overall atmospheric pressure of 65 bar. At IW +0, the strong influence of redox-dependent carbonate partitioning and lower outgassing rates of water from a reduced melt result in surface pressures much lower than those observed today; CO<sub>2</sub> values are low, and the atmosphere would be dominated by H<sub>2</sub>O and N<sub>2</sub>. However, at IW +2, the values are much closer to current observations. Subsequently, H<sub>2</sub>O would undergo photodissociation followed by H<sub>2</sub> escape, while the remaining oxygen would react with CH<sub>4</sub> to form more CO<sub>2</sub>, potentially leading to an oxidized atmosphere similar to today's. Therefore, if carbonate partitioning effects are as significant as suggested by our model, an oxidation state closer to IW +2 for Venus's mantle is likely. It is important to note that oxygen fugacity may change over time, and some studies have shown that carbon can still partition into the melt at low oxygen fugacities and higher pressures as CH<sub>4</sub> fluids if sufficient H<sub>2</sub> is present (Gaillard et al., 2022). Both effects will be explored in future work.

Despite the increased availability of data on Mars, determining the mantle's redox state remains a significant challenge. Deng et al. (2020)

proposed a redox state of IW  $-0.3$  for the top of the Martian magma ocean, with more reducing conditions at the bottom. However, Martian rocks are observed to be more oxidized (see Table 1). For our study, we set the volatile content in the Martian mantle at 290 ppm  $\text{H}_2\text{O}$ , which is the upper limit proposed by McCubbin et al. (2012). Hirschmann and Withers (2008) indicated that the Martian melt carbon content ranges between 0.01 and 0.1 wt%. By back-calculating from Eq. (1), we assume a carbon content of 100 ppm and set nitrogen at 10 ppm. We established a surface melt flux of  $2 \times 10^{13} \text{ kg yr}^{-1}$ , which is 20% of the estimated flux for Archean Earth according to Guimond et al. (2021) and varied the oxygen fugacity between IW +0 and IW +2. At an oxygen fugacity of IW +0 and surface temperatures between 200 and 300 K, the atmosphere was dominated by  $\text{NH}_3$  and  $\text{CH}_4$  with partial pressures of 0.45 bar and 0.07 bar, respectively, resulting in a rainout of an equivalent global layer of 77 m. Conversely, at IW +2, the atmosphere was dominated by  $\text{CO}_2$  with up to 3.8 bar, 0.5 bar  $\text{N}_2$ , and 0.6 bar  $\text{CH}_4$ , yielding a global water layer equivalent of 155 m, which aligns with the values proposed by Carr and Head (2003). Our model calculations indicated an atmospheric pressure range of 0.5 to 5 bar, consistent with the values proposed by Hirschmann and Withers (2008) (70 mbar to 13 bar), although some studies have suggested higher atmospheric pressures up to 100 bar (Elkins-Tanton, 2008).

Lastly, Earth's atmospheric composition with its high oxygen levels deviates the most from our model predictions, which can be attributed to Earth's extensive biological activity. By setting the oxygen fugacity to IW +1.5, the surface temperature to 290 K, and surface melt flux to  $1 \times 10^{14} \text{ kg yr}^{-1}$ , our model calculates an atmospheric pressure of 4.6 bar after 1 Gy with  $P_{\text{N}_2} = 1$  bar,  $P_{\text{CO}_2} = 0.9$  bar, and  $P_{\text{CH}_4} = 2.7$  bar which is generally in agreement with the results published by Catling and Zahnle (2020), except for the high  $\text{CH}_4$  levels which might be overestimated in our model due to the long equilibration time of  $\text{CH}_4$  (Liggins et al., 2023), which is not considered in the model. In our model, 167.656 million  $\text{km}^3$  of water are condensed from degassed  $\text{H}_2\text{O}$  over a period of 1 Gyrs, which constitutes approximately 12% of the current volume of Earth's hydrosphere. Consequently, this estimate appears to be underestimated, particularly given that Korenaga (2008) suggested the Archean oceans contained twice as much water as they do today. Several factors could explain this discrepancy in water abundance: (1) substantial amounts of water may have been degassed into the atmosphere during the magma ocean phase, (2) our estimates for  $\text{H}_2\text{O}$  content in the mantle and melt may be too low, (3) processes other than  $\text{H}_2\text{O}$  degassing contributed to the formation of Earth's oceans, or (4) as shown by Dorn et al. (2018), the mantle's higher temperature during the Archean limited its water retention capacity, redistributing excess water to the oceans.

In summary, our results suggest that the terrestrial planets in the solar system would have type C secondary atmospheres regardless of whether they had the same initial volatile inventory through gravitational scattering or exhibited variations in volatile content. This includes differences in the abundance of  $\text{H}_2\text{O}$  due to their positions in the accretional disk. The primary distinction would lie in the relative abundance of each component ( $\text{CO}_2$ ,  $\text{CH}_4$ ,  $\text{H}_2\text{O}$ , and  $\text{N}_2$ ). Additionally, our analysis suggests that had life and plate tectonics not influenced Earth, its atmospheric composition today would likely resemble that of Mars and Venus. Our model indicates that the differing atmospheric pressures and temperatures observed on these planets stem from variations in their distance from the sun and their distinct sizes, resulting in varying levels of melt production. Despite Venus experiencing significantly higher solar radiation, its dense  $\text{CO}_2$ -dominated atmosphere and cloud cover shielded it from substantial atmospheric loss, since  $\text{CO}_2$  acts as an infrared cooler in the thermosphere and lowers the base of the thermosphere to about 200 km (Way et al., 2023). Conversely, Mars, due to its smaller size and lower melt production likely never attained or maintained substantial atmospheric pressures. Mars likely experienced efficient atmospheric loss due to its low gravity, as the ions in its atmosphere needed less acceleration to escape (Way et al., 2023). This, combined with its low initial atmospheric pressure, resulted in the low atmospheric pressures observed today.

#### 4.3. Stellar luminosity, planet size and planet distance

To explore the diverse evolutionary paths of Venus, Earth, and Mars, as well as to extrapolate implications for exoplanetary systems, we conducted systematic variations in planet size, planet distance from the host star, and additionally, stellar luminosity. In our model, the influence of stellar luminosity and planet distance on surface temperature is not implemented; thus, their effects are solely confined to hydrogen escape dynamics. Focusing on G-type stars ranging from 0.9 to 1.06 solar masses, we tested the effect of planet distance within the range from Venus to the asteroid belt. Additionally, we expanded our analysis to encompass a planetary system orbiting an M dwarf star, akin to Trappist-1. In our investigations, we found that the presence of  $\text{H}_2$  in the atmosphere after 1 Gyrs was highly improbable for planets with intermediate melt production. However, exceptional cases revealed the prevalence of  $\text{H}_2$ , primarily in scenarios involving extremely high melt production. Such conditions, however, necessitate substantial internal heat, which may be achieved on a planet situated close to its host star, hence exposing it to intense stellar winds that would facilitate  $\text{H}_2$  escape. Alternatively, planets influenced by strong tidal forces exerted by massive bodies could also sustain such high levels of internal heat conducive to  $\text{H}_2$  retention (Barnes et al., 2013). Nevertheless, it remains debatable whether such planets would possess adequate internal heat to degas significant quantities of  $\text{H}_2$  initially. Contrary to stellar luminosity and planet distance, variations in planet size, along with the associated melt production rate, exert influence on surface pressure and, consequently, on atmospheric composition. The outcomes for Mars-sized and Earth-sized planets exhibit minimal disparity, with the exception being that lower atmospheric pressure on a Mars-sized planet would result in a higher presence of  $\text{H}_2\text{O}$  in the atmosphere due to the pressure-dependent solubility of water. These assertions, however, remain speculative and require further model refinement for validation.

In conclusion, our model demonstrates that only specific types of volcanically degassed atmospheres exist, each with certain maximum atmospheric pressures. The advent of JWST ushers in a new era of atmospheric characterization, allowing us to test and refine our models with precise observations.

## 5. Conclusions

Our model indicates that mantle oxygen fugacity, melt production rates, and atmospheric temperatures have a significant influence on the composition and pressure of secondary atmospheres below 600 K. Low mantle oxygen fugacities lead to the formation of N-dominated and thin type A atmospheres. Degassing from mantles with high oxygen fugacities will result in  $\text{CO}_2$  or  $\text{H}_2\text{O}$  dominated and thick type C atmospheres, which are likely to have a considerable greenhouse effect.  $\text{CH}_4$  may become the dominant atmospheric species at intermediate oxygen fugacities (IW +0.5 to IW +2) and cold atmospheric temperatures (below 400 K). Furthermore, low atmospheric temperatures favor  $\text{NH}_3$  over  $\text{N}_2$  and lead to the removal of water from the atmosphere through condensation. Melt production rates significantly influence the pressure of the atmosphere as well as the water content, with water being more dominant at low melt production rates due to its increased solubility under high pressures. At elevated melt production rates and strongly reduced conditions,  $\text{H}_2$  degassing may exceed atmospheric loss, leaving a substantial amount of  $\text{H}_2$  in the atmosphere.

### CRedit authorship contribution statement

**Caroline Brachmann:** Writing – original draft, Visualization, Software, Resources, Methodology, Investigation, Formal analysis, Data curation, Conceptualization. **Lena Noack:** Writing – review & editing, Validation, Supervision, Project administration, Funding acquisition, Conceptualization. **Philipp Alexander Baumeister:** Software, Resources. **Frank Sohl:** Writing – review & editing, Validation, Supervision, Project administration, Funding acquisition.

### Declaration of Generative AI and AI-assisted technologies in the writing process

During the preparation of this work the author(s) used ChatGPT in order to enhance wording. After using this tool/service, the author(s) reviewed and edited the content as needed and take(s) full responsibility for the content of the publication.

### Declaration of competing interest

The authors declare that they have no known competing financial interests or personal relationships that could have appeared to influence the work reported in this paper.

### Acknowledgments

This project was funded by the Deutsche Forschungsgemeinschaft (DFG; German Research Foundation) Project-ID 263649064—TRR 170 and by the European Union (ERC, DIVERSE, 101087755). Views and

opinions expressed are however those of the author(s) only and do not necessarily reflect those of the European Union or the European Research Council Executive Agency. Neither the European Union nor the granting authority can be held responsible for them. We want to thank Daniel Kitzmann for his help with implementing Fastchem into our model. We would like to thank Fabrice Gaillard and Oliver Herbert for their insights into atmospheric degassing and re-equilibration. We thank Claire Guimond and two anonymous reviewers for their thorough and constructive reviews, which helped to improve the manuscript substantially.

### Appendix

The following plots show the partial pressure of each atmospheric gas at varying surface temperatures over the period of 1 Gyr for selected runs. The initial parameters are shown in the captions.

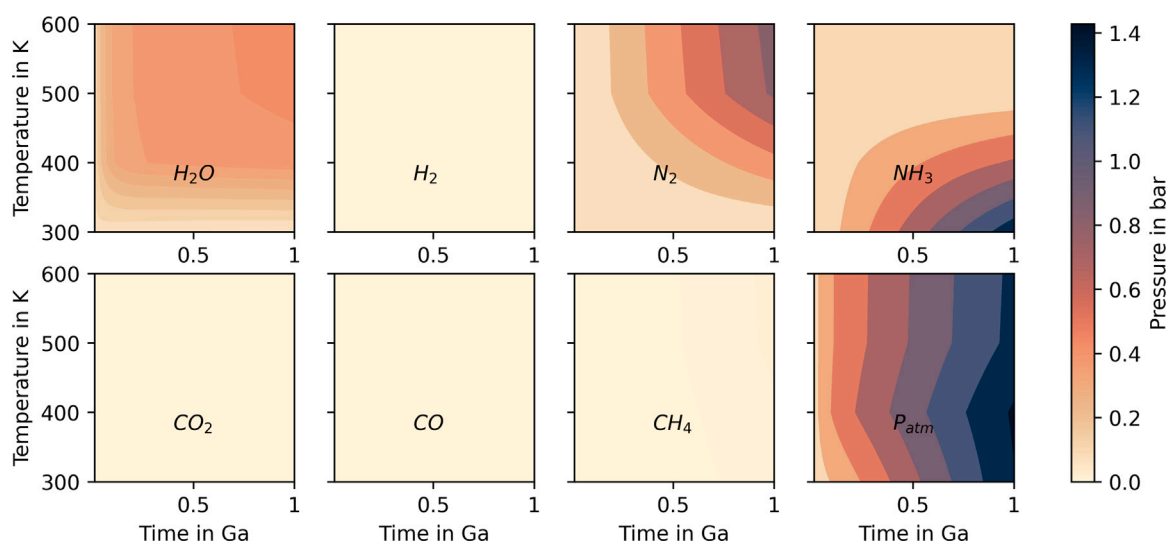


Fig. 5. The volatile content is set to values expected for Earth following magma ocean solidification, with 450 ppm  $\text{H}_2\text{O}$ , 50 ppm  $\text{CO}_2$ , 10 ppm N, and a mantle oxygen fugacity of IW - 1, resulting in a type A atmosphere.

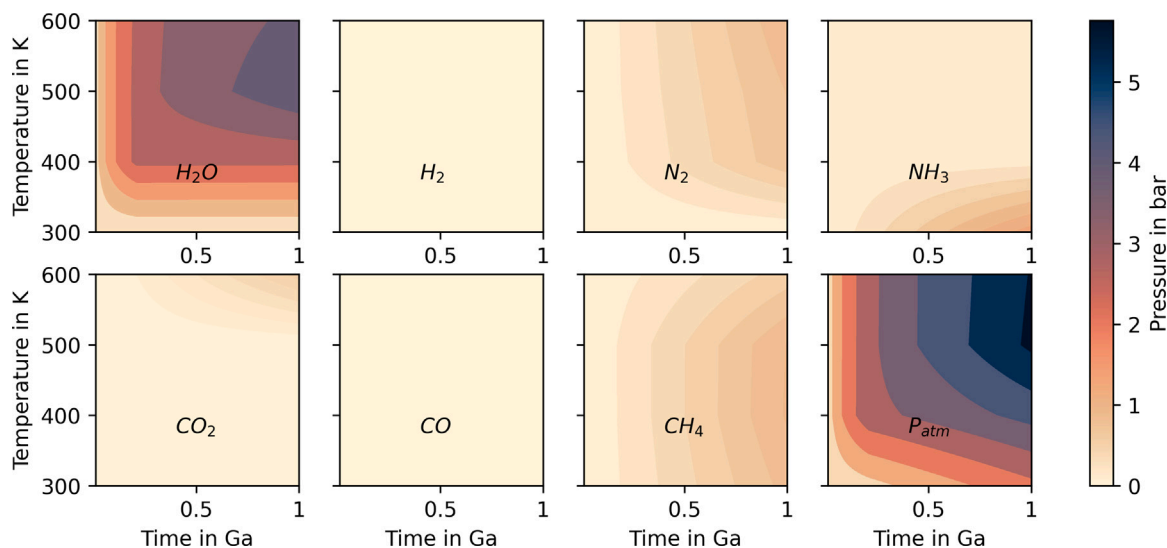


Fig. 6. The volatile content set to values expected for Earth after Magma ocean solidification with 450 ppm  $\text{H}_2\text{O}$ , 50 ppm  $\text{CO}_2$ , 10 ppm N, and a mantle oxygen fugacity IW + 1. Here a shift from a type A atmosphere to a type C atmosphere can be observed around 400 K.

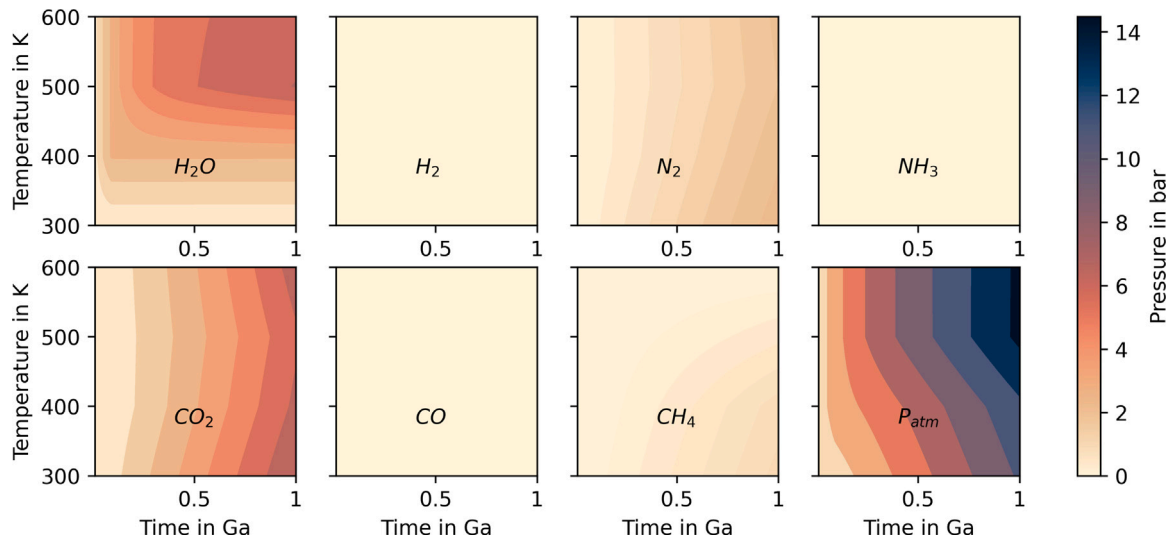


Fig. 7. The volatile content set to values expected for Earth after Magma ocean solidification with 450 ppm H<sub>2</sub>O, 50 ppm CO<sub>2</sub>, 10 ppm N, and a mantle oxygen fugacity IW + 3, resulting in a type C atmosphere.

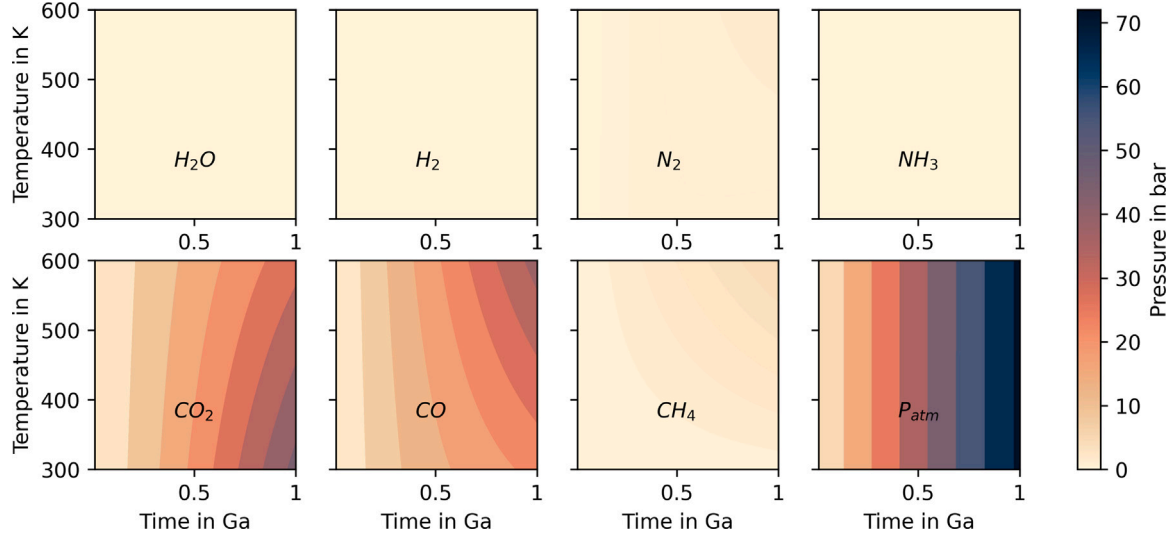


Fig. 8. The volatile content is set for a theoretical H-depleted, C-enriched planet, with 50 ppm H<sub>2</sub>O, 500 ppm CO<sub>2</sub>, 10 ppm N, a mantle oxygen fugacity of IW + 2, while ignoring oxygen fugacity-dependent carbon partitioning and graphite condensation, resulting in a type D atmosphere.

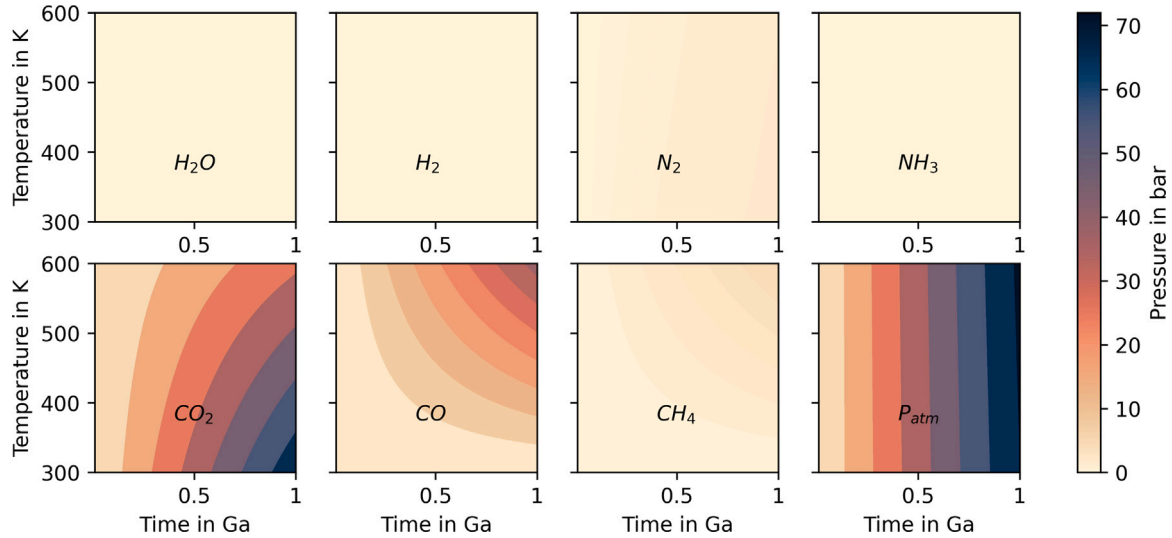


Fig. 9. The volatile content is set for a theoretical H-depleted, C-enriched planet, with 50 ppm H<sub>2</sub>O, 500 ppm CO<sub>2</sub>, 10 ppm N, and a mantle oxygen fugacity of IW + 2, while ignoring oxygen fugacity-dependent carbon partitioning and allowing graphite to condense, resulting in a type D atmosphere above 400 K and a type C atmosphere below 400 K.

## Data availability

Data will be made available on request.

## References

- Albarède, F., 2009. Volatile accretion history of the terrestrial planets and dynamic implications. *Nature* 461 (7268), 1227–1233. <http://dx.doi.org/10.1038/nature08477>.
- Aléon, J., Lévy, D., Aléon-Toppiani, A., Bureau, H., Khodja, H., Brisset, F., 2022. Determination of the initial hydrogen isotopic composition of the solar system. *Nat. Astron.* 6 (4), 458–463. <http://dx.doi.org/10.1038/s41550-021-01595-7>.
- Ardia, P., Hirschmann, M., Withers, A., Stanley, B., 2013. Solubility of CH<sub>4</sub> in a synthetic basaltic melt, with applications to atmosphere–magma ocean–core partitioning of volatiles and to the evolution of the Martian atmosphere. *Geochim. Cosmochim. Acta* 114, 52–71. <http://dx.doi.org/10.1016/j.gca.2013.03.028>.
- Atreya, S.K., Donahue, T.M., Kuhn, W.R., 1978. Evolution of a nitrogen atmosphere on Titan. *Science* 201 (4356), 611–613. <http://dx.doi.org/10.1126/science.201.4356.611>.
- Aubaud, C., Hauri, E.H., Hirschmann, M.M., 2004. Hydrogen partition coefficients between nominally anhydrous minerals and basaltic melts. *Geophys. Res. Lett.* 31 (20). <http://dx.doi.org/10.1029/2004GL021341>, 2004GL021341.
- Barnes, R., Mullins, K., Goldblatt, C., Meadows, V.S., Kasting, J.F., Heller, R., 2013. Tidal Venuses: Triggering a climate catastrophe via tidal heating. *Astrobiology* 13 (3), 225–250. <http://dx.doi.org/10.1089/ast.2012.0851>.
- Basilevsky, A.T., Head, J.W., 2003. The surface of Venus. *Prog. Phys.* 66 (10), 1699–1734. <http://dx.doi.org/10.1088/0034-4885/66/10/R04>.
- Baumeister, P., Tosi, N., Brachmann, C., Grenfell, J.L., Noack, L., 2023. Redox state and interior structure control on the long-term habitability of stagnant-lid planets. *Astron. Astrophys.* 675, A122. <http://dx.doi.org/10.1051/0004-6361/202245791>.
- Blank, J., Stolper, E., Carroll, M., 1993. Solubilities of carbon dioxide and water in rhyolitic melt at 850° C and 750 bars. *Earth Planet. Sci. Lett.* 119 (1), 27–36. [http://dx.doi.org/10.1016/0012-821X\(93\)90004-S](http://dx.doi.org/10.1016/0012-821X(93)90004-S).
- Burcat, A., Ruscic, B., Chemistry, 2005. Third millennium ideal gas and condensed phase thermochemical database for combustion (with update from active thermochemical tables). (ANL-05/20, 925269), pp. ANL-05/20, 925269. <http://dx.doi.org/10.2172/925269>.
- Burkhardt, C., Spitzer, F., Morbidelli, A., Budde, G., Render, J.H., Kruijer, T.S., Kleine, T., 2021. Terrestrial planet formation from lost inner solar system material. *Sci. Adv.* 7 (52), eabj7601. <http://dx.doi.org/10.1126/sciadv.abj7601>.
- Carr, M.H., Head, J.W., 2003. Oceans on Mars: An assessment of the observational evidence and possible fate. *J. Geophys. Res.: Planets* 108, <http://dx.doi.org/10.1029/2002JE001963>, 2002JE001963.
- Carr, M.H., Head, J.W., 2010. Geologic history of Mars. *Earth Planet. Sci. Lett.* 294 (3), 185–203. <http://dx.doi.org/10.1016/j.epsl.2009.06.042>.
- Catling, D.C., Kasting, J.F., 2017. *Atmospheric Evolution on Inhabited and Lifeless Worlds*, first ed. Cambridge University Press, <http://dx.doi.org/10.1017/9781139020558>.
- Catling, D.C., Zahnle, K.J., 2020. The Archean atmosphere. *Sci. Adv.* 6 (9), eaax1420. <http://dx.doi.org/10.1126/sciadv.aax1420>.
- Chambers, J., Wetherill, G., 1998. Making the terrestrial planets: N-body integrations of planetary embryos in three dimensions. *Icarus* 136 (2), 304–327. <http://dx.doi.org/10.1006/icar.1998.6007>.
- Deng, J., Du, Z., Karki, B.B., Ghosh, D.B., Lee, K.K.M., 2020. A magma ocean origin to divergent redox evolutions of rocky planetary bodies and early atmospheres. *Nature Commun.* 11 (1), 2007. <http://dx.doi.org/10.1038/s41467-020-15757-0>.
- Dixon, J.E., Stolper, E.M., Holloway, J.R., 1995. An experimental study of water and carbon dioxide solubilities in mid-ocean ridge basaltic liquids. Part I: Calibration and solubility models. *J. Petrol.* <http://dx.doi.org/10.1093/oxfordjournals.petrology.a037267>.
- Donahue, T.M., Hoffman, J.H., Hodges, R.R., Watson, A.J., 1982. Venus was wet: A measurement of the ratio of deuterium to hydrogen. *Science* 216 (4546), 630–633. <http://dx.doi.org/10.1126/science.216.4546.630>.
- Dorn, C., Noack, L., Rozel, A.B., 2018. Outgassing on stagnant-lid super-earths. *Astron. Astrophys.* 614, A18. <http://dx.doi.org/10.1051/0004-6361/201731513>.
- Dreibus, G., Wänke, H., 1985. Mars, a volatile-rich planet. *Meteoritics* 20, 367, ADS Bibcode: 1985Metic..20..367D.
- Elkins-Tanton, L., 2008. Linked magma ocean solidification and atmospheric growth for Earth and Mars. *Earth Planet. Sci. Lett.* 271 (1), 181–191. <http://dx.doi.org/10.1016/j.epsl.2008.03.062>.
- Elkins-Tanton, L.T., 2012. Magma oceans in the inner solar system. *Annu. Rev. Earth Planet. Sci.* 40 (1), 113–139. <http://dx.doi.org/10.1146/annurev-earth-042711-105503>.
- Frost, D.J., McCammon, C.A., 2008. The redox state of Earth's mantle. *Annu. Rev. Earth Planet. Sci.* 36 (1), 389–420. <http://dx.doi.org/10.1146/annurev-earth.36.031207.124322>.
- Gaillard, F., Bouhifd, M.A., Füre, E., Malavergne, V., Marrocchi, Y., Noack, L., Ortenzi, G., Roskosz, M., Vulpius, S., 2021. The diverse planetary ingassing/outgassing paths produced over billions of years of magmatic activity. *Space Sci. Rev.* 217 (1), 22. <http://dx.doi.org/10.1007/s11214-021-00802-1>.
- Gaillard, F., Malavergne, V., Bouhifd, M.A., Rogerie, G., 2022. A speciation model linking the fate of carbon and hydrogen during core – magma ocean equilibration. *Earth Planet. Sci. Lett.* 577, 117266. <http://dx.doi.org/10.1016/j.epsl.2021.117266>.
- Gaillard, F., Scaillet, B., 2014. A theoretical framework for volcanic degassing chemistry in a comparative planetology perspective and implications for planetary atmospheres. *Earth Planet. Sci. Lett.* 403, 307–316. <http://dx.doi.org/10.1016/j.epsl.2014.07.009>.
- Gaillard, F., Schmidt, B., Mackwell, S., McCammon, C., 2003. Rate of hydrogen–iron redox exchange in silicate melts and glasses. *Geochim. Cosmochim. Acta* 67 (13), 2427–2441. [http://dx.doi.org/10.1016/S0016-7037\(02\)01407-2](http://dx.doi.org/10.1016/S0016-7037(02)01407-2).
- Gardner, J.E., Hilton, M., Carroll, M.R., 1999. Experimental constraints on degassing of magma: isothermal bubble growth during continuous decompression from high pressure. *Earth Planet. Sci. Lett.* 168 (1), 201–218. [http://dx.doi.org/10.1016/S0012-821X\(99\)00051-5](http://dx.doi.org/10.1016/S0012-821X(99)00051-5).
- Genda, H., Abe, Y., 2005. Enhanced atmospheric loss on protoplanets at the giant impact phase in the presence of oceans. *Nature* 433 (7028), 842–844. <http://dx.doi.org/10.1038/nature03360>.
- Gillmann, C., Chassefière, E., Lognonné, P., 2009. A consistent picture of early hydrodynamic escape of Venus atmosphere explaining present Ne and Ar isotopic ratios and low oxygen atmospheric content. *Earth Planet. Sci. Lett.* 286 (3), 503–513. <http://dx.doi.org/10.1016/j.epsl.2009.07.016>.
- Gillmann, C., Tackley, P., 2014. Atmosphere/mantle coupling and feedbacks on Venus. *J. Geophys. Res.: Planets* 119 (6), 1189–1217. <http://dx.doi.org/10.1002/2013JE004505>.
- Glein, C.R., 2015. Noble gases, nitrogen, and methane from the deep interior to the atmosphere of Titan. *Icarus* 250, 570–586. <http://dx.doi.org/10.1016/j.icarus.2015.01.001>.
- Glein, C.R., Desch, S.J., Shock, E.L., 2009. The absence of endogenic methane on Titan and its implications for the origin of atmospheric nitrogen. *Icarus* 204 (2), 637–644. <http://dx.doi.org/10.1016/j.icarus.2009.06.020>.
- Grenfell, J.L., Gebauer, S., Godolt, M., Stracke, B., Lehmann, R., Rauer, H., 2018. Limitation of atmospheric composition by combustion–explosion in exoplanetary atmospheres. *Astrophys. J.* 861 (1), 38. <http://dx.doi.org/10.3847/1538-4357/aab2a9>.
- Grott, M., Morschhauser, A., Breuer, D., Hauber, E., 2011. Volcanic outgassing of CO<sub>2</sub> and H<sub>2</sub>O on Mars. *Earth Planet. Sci. Lett.* 308 (3), 391–400. <http://dx.doi.org/10.1016/j.epsl.2011.06.014>.
- Guimond, C.M., Noack, L., Ortenzi, G., Sohl, F., 2021. Low volcanic outgassing rates for a stagnant lid Archean Earth with graphite-saturated magmas. *Phys. Earth Planet. Inter.* 320, 106788. <http://dx.doi.org/10.1016/j.pepi.2021.106788>.
- Haberle, R., 2003. Planetary atmospheres | mars. In: *Encyclopedia of Atmospheric Sciences*. Elsevier, pp. 1745–1755. <http://dx.doi.org/10.1016/B0-12-227090-8/00312-2>.
- Hamano, K., Abe, Y., Genda, H., 2013. Emergence of two types of terrestrial planet on solidification of magma ocean. *Nature* 497 (7451), 607–610. <http://dx.doi.org/10.1038/nature12163>.
- Hier-Majumder, S., Hirschmann, M.M., 2017. The origin of volatiles in the Earth's mantle. *Geochim. Geophys. Geosyst.* 18 (8), 3078–3092. <http://dx.doi.org/10.1002/2017GC006937>.
- Hirschmann, M.M., 2012. Magma ocean influence on early atmosphere mass and composition. *Earth Planet. Sci. Lett.* 341–344, 48–57. <http://dx.doi.org/10.1016/j.epsl.2012.06.015>.
- Hirschmann, M.M., Withers, A.C., 2008. Ventilation of CO<sub>2</sub> from a reduced mantle and consequences for the early Martian greenhouse. *Earth Planet. Sci. Lett.* 270 (1), 147–155. <http://dx.doi.org/10.1016/j.epsl.2008.03.034>.
- Holloway, J.R., Pan, V., Gudmundson, G., 1992. High-pressure fluid-absent melting experiments in the presence of graphite; oxygen fugacity, ferric/ferrous ratio and dissolved CO<sub>2</sub>. *Eur. J. Mineral.* 4, 105–114.
- Holtz, F., Behrens, H., Dingwell, D.B., Johannes, W., 1995. H<sub>2</sub>O solubility in haplogranitic melts; compositional, pressure, and temperature dependence. *Am. Mineral.* 80 (1), 94–108. <http://dx.doi.org/10.2138/am-1995-1-210>.
- Hörst, S.M., 2017. Titan's atmosphere and climate. *J. Geophys. Res.: Planets* 122 (3), 432–482. <http://dx.doi.org/10.1002/2016JE005240>.
- Johansen, A., Ronnet, T., Bizzarro, M., Schiller, M., Lambrechts, M., Nordlund, Å., Lammer, H., 2021. A pebble accretion model for the formation of the terrestrial planets in the solar system. *Sci. Adv.* 7 (8), eabc0444. <http://dx.doi.org/10.1126/sciadv.abc0444>.
- Johnstone, C.P., Güdel, M., Lammer, H., Kislyakova, K.G., 2018. Upper atmospheres of terrestrial planets: Carbon dioxide cooling and the earth's thermospheric evolution. *Astron. Astrophys.* 617, A107. <http://dx.doi.org/10.1051/0004-6361/201832776>.
- Kasting, J.F., 1988. Runaway and moist greenhouse atmospheres and the evolution of Earth and Venus. *Icarus* 74 (3), 472–494. [http://dx.doi.org/10.1016/0019-1035\(88\)90116-9](http://dx.doi.org/10.1016/0019-1035(88)90116-9).
- Katyal, N., Ortenzi, G., Lee Grenfell, J., Noack, L., Sohl, F., Godolt, M., García Muñoz, A., Schreier, F., Wunderlich, F., Rauer, H., 2020. Effect of mantle oxidation state and escape upon the evolution of earth's magma ocean atmosphere. *Astron. Astrophys.* 643, A81. <http://dx.doi.org/10.1051/0004-6361/202038779>.

- Katz, R.F., Spiegelman, M., Langmuir, C.H., 2003. A new parameterization of hydrous mantle melting. *Geochem. Geophys. Geosyst.* 4 (9), <http://dx.doi.org/10.1029/2002GC000433>, 2002GC000433.
- Kepler, H., Golabek, G., 2019. Graphite floatation on a magma ocean and the fate of carbon during core formation. *Geochem. Perspect. Lett.* 12–17. <http://dx.doi.org/10.7185/geochemlet.1918>.
- Kite, E.S., Barnett, M.N., 2020. Exoplanet secondary atmosphere loss and revival. *Proc. Natl. Acad. Sci.* 117 (31), 18264–18271. <http://dx.doi.org/10.1073/pnas.2006177117>.
- Kite, E.S., Manga, M., Gaidos, E., 2009. Geodynamics and rate of volcanism on massive earth-like planets. *Astrophys. J.* 700 (2), 1732–1749. <http://dx.doi.org/10.1088/0004-637X/700/2/1732>.
- Kleine, T., Budde, G., Burkhardt, C., Kruijjer, T.S., Worsham, E.A., Morbidelli, A., Nimmo, F., 2020. The non-carbonaceous–carbonaceous meteorite dichotomy. *Space Sci. Rev.* 216 (4), 55. <http://dx.doi.org/10.1007/s11214-020-00675-w>.
- Korenaga, J., 2008. Plate tectonics, flood basalts and the evolution of Earth's oceans. *Terra Nova* 20 (6), 419–439. <http://dx.doi.org/10.1111/j.1365-3121.2008.00843.x>.
- Krissansen-Totton, J., Fortney, J.J., Nimmo, F., 2021. Was Venus ever habitable? Constraints from a coupled interior–atmosphere–redox evolution model. *Planet. Sci. J.* 2 (5), 216. <http://dx.doi.org/10.3847/PSJ/ac2580>.
- Krissansen-Totton, J., Olson, S., Catling, D.C., 2018. Disequilibrium biosignatures over Earth history and implications for detecting exoplanet life. *Sci. Adv.* 4 (1), eaao5747. <http://dx.doi.org/10.1126/sciadv.aao5747>.
- Kulikov, Y., Lammer, H., Lichtenegger, H., Terada, N., Ribas, I., Kolb, C., Langmayr, D., Lundin, R., Guinan, E., Barabash, S., Biernat, H., 2006. Atmospheric and water loss from early Venus. *Planet. Space Sci.* 54 (13), 1425–1444. <http://dx.doi.org/10.1016/j.pss.2006.04.021>.
- Lewis, J.S., 1971. Satellites of the outer planets: Their physical and chemical nature. *Icarus* 15 (2), 174–185. [http://dx.doi.org/10.1016/0019-1035\(71\)90072-8](http://dx.doi.org/10.1016/0019-1035(71)90072-8).
- Li, Y., Wiedenbeck, M., Shcheka, S., Kepler, H., 2013. Nitrogen solubility in upper mantle minerals. *Earth Planet. Sci. Lett.* 377–378, 311–323. <http://dx.doi.org/10.1016/j.epsl.2013.07.013>.
- Libourel, G., Marty, B., Humbert, F., 2003. Nitrogen solubility in basaltic melt. Part I. Effect of oxygen fugacity. *Geochim. Cosmochim. Acta* 67 (21), 4123–4135. [http://dx.doi.org/10.1016/S0016-7037\(03\)00259-X](http://dx.doi.org/10.1016/S0016-7037(03)00259-X).
- Lichtenberg, T., Bower, D.J., Hammond, M., Boukrouche, R., Sanan, P., Tsai, S.-M., Pierrehumbert, R.T., 2021. Vertically resolved magma ocean–protoatmosphere evolution:  $H_2$ ,  $H_2O$ ,  $CO_2$ ,  $CH_4$ ,  $CO$ ,  $O_2$ , and  $N_2$  as primary absorbers. *J. Geophys. Res.: Planets* 126 (2), <http://dx.doi.org/10.1029/2020JE006711>, e2020JE006711.
- Lichtenegger, H.I.M., Kislyakova, K.G., Odert, P., Erkaev, N.V., Lammer, H., Gröller, H., Johnstone, C.P., Elkins-Tanton, L., Tu, L., Güdel, M., Holmström, M., 2016. Solar XUV and ENA-driven water loss from early Venus' steam atmosphere. *J. Geophys. Res. Space Phys.* 121 (5), 4718–4732. <http://dx.doi.org/10.1002/2015JA022226>.
- Liggins, P., Jordan, S., Rimmer, P.B., Shorttle, O., 2022. Growth and evolution of secondary volcanic atmospheres: I. Identifying the geological character of hot rocky planets. *J. Geophys. Res.: Planets* 127 (7), <http://dx.doi.org/10.1029/2021JE007123>, e2021JE007123.
- Liggins, P., Jordan, S., Rimmer, P.B., Shorttle, O., 2023. Growth and evolution of secondary volcanic atmospheres: II. The importance of kinetics. *J. Geophys. Res.: Planets* 128 (3), <http://dx.doi.org/10.1029/2022JE007528>, e2022JE007528.
- Liu, Y., Zhang, Y., Behrens, H., 2005. Solubility of  $H_2O$  in rhyolitic melts at low pressures and a new empirical model for mixed  $H_2O$ – $CO_2$  solubility in rhyolitic melts. *J. Volcanol. Geotherm. Res.* 143 (1), 219–235. <http://dx.doi.org/10.1016/j.jvolgeores.2004.09.019>.
- Luger, R., Barnes, R., 2015. Extreme water loss and abiotic  $O_2$  buildup on planets throughout the habitable zones of M dwarfs. *Astrobiology* 15 (2), 119–143. <http://dx.doi.org/10.1089/ast.2014.1231>.
- Mandt, K.E., Waite, J.H., Teolis, B., Magee, B.A., Bell, J., Westlake, J.H., Nixon, C.A., Mousis, O., Lunine, J.I., 2012. The  $^{12}C/^{13}C$  ratio on Titan from *Cassini* INMS measurements and implications for the evolution of methane. *Astrophys. J.* 749 (2), 160. <http://dx.doi.org/10.1088/0004-637X/749/2/160>.
- Marty, B., 2012. The origins and concentrations of water, carbon, nitrogen and noble gases on Earth. *Earth Planet. Sci. Lett.* 313–314, 56–66. <http://dx.doi.org/10.1016/j.epsl.2011.10.040>.
- McCubbin, F.M., Riner, M.A., Vander Kaaden, K.E., Burkemper, L.K., 2012. Is Mercury a volatile-rich planet? *Geophys. Res. Lett.* 39 (9), <http://dx.doi.org/10.1029/2012GL051711>, 2012GL051711.
- Moore, G., Carmichael, I.S.E., 1998. The hydrous phase equilibria (to 3 kbar) of an andesite and basaltic andesite from western Mexico: constraints on water content and conditions of phenocryst growth. *Contributions Mineral. Petrol.* 130 (3), 304–319. <http://dx.doi.org/10.1007/s004100050367>.
- Morbidelli, A., Chambers, J., Lunine, J.I., Petit, J.M., Robert, F., Valsecchi, G.B., Cyr, K.E., 2000. Source regions and timescales for the delivery of water to the Earth. *Meteorit. Planet. Sci.* 35 (6), 1309–1320. <http://dx.doi.org/10.1111/j.1945-5100.2000.tb01518.x>.
- Morbidelli, A., Lunine, J., O'Brien, D., Raymond, S., Walsh, K., 2012. Building terrestrial planets. *Annu. Rev. Earth Planet. Sci.* 40 (1), 251–275. <http://dx.doi.org/10.1146/annurev-earth-042711-105319>.
- Moses, J.I., Line, M.R., Visscher, C., Richardson, M.R., Nettelmann, N., Fortney, J.J., Barman, T.S., Stevenson, K.B., Madhusudhan, N., 2013. Compositional diversity in the atmospheres of hot neptunes, with application to GJ 436b. *Astrophys. J.* 777 (1), 34. <http://dx.doi.org/10.1088/0004-637X/777/1/34>.
- Mysen, B.O., Arculus, R.J., Eggler, D.H., 1975. Solubility of carbon dioxide in melts of andesite, tholeiite, and olivine nephelinite composition to 30 kbar pressure. *Contributions Mineral. Petrol.* 53 (4), 227–239. <http://dx.doi.org/10.1007/BF00382441>.
- Nicklas, R.W., Puchtel, I.S., Ash, R.D., Piccoli, P.M., Hanski, E., Nisbet, E.G., Water-ton, P., Pearson, D.G., Anbar, A.D., 2019. Secular mantle oxidation across the Archean-Proterozoic boundary: Evidence from V partitioning in komatiites and picrites. *Geochim. Cosmochim. Acta* 250, 49–75. <http://dx.doi.org/10.1016/j.gca.2019.01.037>.
- Nixon, C.A., Temelso, B., Viatier, S., Teanby, N.A., Bézard, B., Achterberg, R.K., Mandt, K.E., Sherrill, C.D., Irwin, P.G.J., Jennings, D.E., Romani, P.N., Coustenis, A., Flasar, F.M., 2012. Isotopic ratios in Titan's methane: Measurements and modeling. *Astrophys. J.* 749 (2), 159. <http://dx.doi.org/10.1088/0004-637X/749/2/159>.
- Noack, L., Breuer, D., Spohn, T., 2012. Coupling the atmosphere with interior dynamics: Implications for the resurfacing of Venus. *Icarus* 217 (2), 484–498. <http://dx.doi.org/10.1016/j.icarus.2011.08.026>.
- Noack, L., Rivoldini, A., Van Hoolst, T., 2017. Volcanism and outgassing of stagnant-lid planets: Implications for the habitable zone. *Phys. Earth Planet. Inter.* 269, 40–57. <http://dx.doi.org/10.1016/j.pepi.2017.05.010>.
- Obrien, D., Morbidelli, A., Levison, H., 2006. Terrestrial planet formation with strong dynamical friction. *Icarus* 184 (1), 39–58. <http://dx.doi.org/10.1016/j.icarus.2006.04.005>.
- O'Brien, D.P., Walsh, K.J., Morbidelli, A., Raymond, S.N., Mandell, A.M., 2014. Water delivery and giant impacts in the 'Grand Tack' scenario. *Icarus* 239, 74–84. <http://dx.doi.org/10.1016/j.icarus.2014.05.009>.
- Odert, P., Lammer, H., Erkaev, N., Nikolaou, A., Lichtenegger, H., Johnstone, C., Kislyakova, K., Leitzinger, M., Tosi, N., 2018. Escape and fractionation of volatiles and noble gases from Mars-sized planetary embryos and growing protoplanets. *Icarus* 307, 327–346. <http://dx.doi.org/10.1016/j.icarus.2017.10.031>.
- Ortenzi, G., Noack, L., Sohl, F., Guimond, C.M., Grenfell, J.L., Dorn, C., Schmidt, J.M., Vulpius, S., Katyal, N., Kitzmann, D., Rauer, H., 2020. Mantle redox state drives outgassing chemistry and atmospheric composition of rocky planets. *Sci. Rep.* 10 (1), 10907. <http://dx.doi.org/10.1038/s41598-020-67751-7>.
- Pan, V., Holloway, J.R., Hervig, R.L., 1991. The pressure and temperature dependence of carbon dioxide solubility in tholeiitic basalt melts. *Geochim. Cosmochim. Acta* 55 (6), 1587–1595. [http://dx.doi.org/10.1016/0016-7037\(91\)90130-W](http://dx.doi.org/10.1016/0016-7037(91)90130-W).
- Raymond, S.N., 2021. A terrestrial convergence. *Nat. Astron.* 5 (9), 875–876. <http://dx.doi.org/10.1038/s41550-021-01488-9>.
- Raymond, S.N., Izidoro, A., 2017. Origin of water in the inner solar system: Planetesimals scattered inward during Jupiter and Saturn's rapid gas accretion. *Icarus* 297, 134–148. <http://dx.doi.org/10.1016/j.icarus.2017.06.030>.
- Raymond, S.N., O'Brien, D.P., Morbidelli, A., Kaib, N.A., 2009. Building the terrestrial planets: Constrained accretion in the inner solar system. *Icarus* 203 (2), 644–662. <http://dx.doi.org/10.1016/j.icarus.2009.05.016>.
- Raymond, S.N., Quinn, T., Lunine, J.I., 2004. Making other Earths: dynamical simulations of terrestrial planet formation and water delivery. *Icarus* 168 (1), 1–17. <http://dx.doi.org/10.1016/j.icarus.2003.11.019>.
- Ronco, M.P., De Elía, G.C., 2014. Diversity of planetary systems in low-mass disks: Terrestrial-type planet formation and water delivery. *Astron. Astrophys.* 567, A54. <http://dx.doi.org/10.1051/0004-6361/201323313>.
- Ronco, M.P., de Elía, G.C., 2018. Formation of solar system analogues – II. Post-gas-phase growth and water accretion in extended discs via N-body simulations. *Mon. Not. R. Astron. Soc.* 479 (4), 5362–5384. <http://dx.doi.org/10.1093/mnras/sty1773>.
- Ronco, M.P., De Elía, G.C., Guilera, O.M., 2015. Terrestrial-type planet formation: Comparing different types of initial conditions. *Astron. Astrophys.* 584, A47. <http://dx.doi.org/10.1051/0004-6361/201526367>.
- Saha, K., 2008. *The Earth's Atmosphere: its Physics and Dynamics*. Springer, OCLC: ocn213114189.
- Saul, A., Wagner, W., 1987. International equations for the saturation properties of ordinary water substance. *J. Phys. Chem. Ref. Data* 16 (4), 893–901. <http://dx.doi.org/10.1063/1.555787>.
- Silver, L.A., Ihinger, P.D., Stolper, E., 1990. The influence of bulk composition on the speciation of water in silicate glasses. *Contributions Mineral. Petrol.* 104 (2), 142–162. <http://dx.doi.org/10.1007/BF00306439>.
- Sleep, N.H., Zahnle, K.J., Lupu, R.E., 2014. Terrestrial aftermath of the Moon-forming impact. *Phil. Trans. R. Soc. A* 372 (2024), 20130172. <http://dx.doi.org/10.1098/rsta.2013.0172>.
- Stock, J.W., Kitzmann, D., Patzer, A.B.C., 2022. FastChem 2: an improved computer program to determine the gas-phase chemical equilibrium composition for arbitrary element distributions. *Mon. Not. R. Astron. Soc.* 517 (3), 4070–4080. <http://dx.doi.org/10.1093/mnras/stac2623>.

- Stolper, E., Holloway, J.R., 1988. Experimental determination of the solubility of carbon dioxide in molten basalt at low pressure. *Earth Planet. Sci. Lett.* 87 (4), 397–408. [http://dx.doi.org/10.1016/0012-821X\(88\)90004-0](http://dx.doi.org/10.1016/0012-821X(88)90004-0).
- Strobel, D.F., Shemansky, D.E., 1982. EUV emission from Titan's upper atmosphere: Voyager 1 encounter. *J. Geophys. Res. Space Phys.* 87, 1361–1368. <http://dx.doi.org/10.1029/JA087iA03p01361>.
- Taylor, F., Grinspoon, D., 2009. Climate evolution of Venus. *J. Geophys. Res.: Planets* 114, <http://dx.doi.org/10.1029/2008JE003316>, 2008JE003316.
- Thompson, M.A., Krissansen-Totton, J., Wogan, N., Telus, M., Fortney, J.J., 2022. The case and context for atmospheric methane as an exoplanet biosignature. *Proc. Natl. Acad. Sci.* 119 (14), e2117933119. <http://dx.doi.org/10.1073/pnas.2117933119>.
- Vulpius, S., Noack, L., 2022. Intrusive magmatism strongly contributed to the volatile release into the atmosphere of early Earth. *Geochem. Geophys. Geosyst.* 23 (12), <http://dx.doi.org/10.1029/2021GC010230>, e2021GC010230.
- Wadhwa, M., 2008. Redox conditions on small bodies, the Moon and Mars. *Rev. Mineral. Geochem.* 68 (1), 493–510. <http://dx.doi.org/10.2138/rmg.2008.68.17>.
- Walsh, K.J., Morbidelli, A., 2011. The effect of an early planetesimal-driven migration of the giant planets on terrestrial planet formation. *Astron. Astrophys.* 526, A126. <http://dx.doi.org/10.1051/0004-6361/201015277>.
- Walsh, K.J., Morbidelli, A., Raymond, S.N., O'Brien, D.P., Mandell, A.M., 2011. A low mass for Mars from Jupiter's early gas-driven migration. *Nature* 475 (7355), 206–209. <http://dx.doi.org/10.1038/nature10201>.
- Way, M.J., Del Genio, A.D., 2020. Venusian habitable climate scenarios: Modeling Venus through time and applications to slowly rotating Venus-like exoplanets. *J. Geophys. Res.: Planets* 125 (5), <http://dx.doi.org/10.1029/2019JE006276>, e2019JE006276.
- Way, M.J., Ostberg, C., Foley, B.J., Gillmann, C., Höning, D., Lammer, H., O'Rourke, J., Persson, M., Plesa, A.-C., Salvador, A., Scherf, M., Weller, M., 2023. Synergies between Venus & exoplanetary observations: Venus and its extrasolar siblings. *Space Sci. Rev.* 219 (1), 13. <http://dx.doi.org/10.1007/s11214-023-00953-3>.
- Wilson, E.H., Atreya, S.K., 2004. Current state of modeling the photochemistry of Titan's mutually dependent atmosphere and ionosphere. *J. Geophys. Res.: Planets* 109, <http://dx.doi.org/10.1029/2003JE002181>, 2003JE002181.
- Woitke, P., Herbort, O., Helling, C., Stüeken, E., Dominik, M., Barth, P., Samra, D., 2021. Coexistence of CH<sub>4</sub>, CO<sub>2</sub>, and H<sub>2</sub>O in exoplanet atmospheres. *Astron. Astrophys.* 646, A43. <http://dx.doi.org/10.1051/0004-6361/202038870>.
- Yamashita, S., 1999. Experimental study of the effect of temperature on water solubility in natural rhyolite melt to 100 MPa. *J. Petrol.* 40 (10), 1497–1507. <http://dx.doi.org/10.1093/etroj/40.10.1497>.
- Yoshioka, T., Nakashima, D., Nakamura, T., Shcheka, S., Keppler, H., 2019. Carbon solubility in silicate melts in equilibrium with a CO-CO<sub>2</sub> gas phase and graphite. *Geochim. Cosmochim. Acta* 259, 129–143. <http://dx.doi.org/10.1016/j.gca.2019.06.007>.
- Yung, Y.L., Allen, M., Pinto, J.P., 1984. Photochemistry of the atmosphere of Titan - comparison between model and observations. *Astrophys. J. Suppl. Ser.* 55, 465. <http://dx.doi.org/10.1086/190963>.
- Zahnle, K.J., Lupu, R., Dobrovolskis, A., Sleep, N.H., 2015. The tethered Moon. *Earth Planet. Sci. Lett.* 427, 74–82. <http://dx.doi.org/10.1016/j.epsl.2015.06.058>.
- Zain, P.S., De Elía, G.C., Ronco, M.P., Guilera, O.M., 2018. Planetary formation and water delivery in the habitable zone around solar-type stars in different dynamical environments. *Astron. Astrophys.* 609, A76. <http://dx.doi.org/10.1051/0004-6361/201730848>.